Chemical Science

ROYAL SOCIETY OF CHEMISTRY

REVIEW

View Article Online
View Journal | View Issue

Cite this: *Chem. Sci.*, 2026, **17**, 6345

Engineering manganese-based cathodes for low-cost and high-energy rechargeable batteries

Hongyu Zhang,[abc] Tingzhou Yang,*[b] Quan Zhou,[ab] Xiaoen Wang*[a] and Zhongwei Chen *[a]

Manganese (Mn)-based cathode materials are emerging as strong candidates for next-generation low-cost rechargeable batteries due to their high energy density, natural abundance, and environmental benignity. However, severe performance degradation caused by voltage decay, transition metal dissolution, and sluggish reaction kinetics has hindered their further commercialization for decades. Herein, we systematically review the composition, electrochemical behavior, and degradation mechanisms of representative Mn-based cathodes in both lithium- and sodium-ion batteries. State-of-the-art optimization strategies are summarized that mitigate key limitations while enhancing electrochemical performance. Advanced *in situ*/operational characterization and theoretical modeling techniques are valued for their role in revealing degradation pathways and guiding rational design. Additionally, techno-economic analysis and life-cycle assessment are introduced to evaluate the feasibility of Mn-based cathodes for sustainable energy storage, which outlines a roadmap for advancing Mn-based cathodes from fundamental research to commercial deployment.

Received 17th December 2025
Accepted 26th January 2026

DOI: 10.1039/d5sc09895e

rsc.li/chemical-science

1 Introduction

The advancement of high-performance energy storage systems is essential to enable renewable energy integration, reduce greenhouse gas emission, and accelerate global decarbonization with co-benefits for society and the economy. To realize these objectives, the development of low-cost, high-energy-density rechargeable batteries is pivotal for achieving a sustainable society.[1–4] Notably, the battery performance metrics are predominantly governed by the cathode material, which constitutes approximately 50% of the total battery material cost.[5] Currently, most commercial cathode materials rely on cobalt or iron-based compounds, each presenting significant limitations. While cobalt-based cathodes demonstrate excellent energy storage potential and structural stability, geological constraints pose serious concerns. According to the latest data from the United States Geological Survey, the abundance of cobalt in the earth's crust is only 25 ppm, rendering it insufficient to meet escalating energy storage demands and resulting in dramatic price volatility.[6] Conversely, iron-based cathodes, despite their natural abundance, are fundamentally constrained by low redox potentials and inferior charge transport characteristics, which collectively restrict their achievable energy density.[5] To enable sustainable expansion of the energy storage market, the development of novel cathode materials that simultaneously offer reduced cost and enhanced energy density represents a critical research priority.

Manganese (Mn)-based cathode materials have recently garnered significant attention due to their low cost, high thermal stability and low toxicity.[7] The crustal abundance of Mn species is much higher than that of nickel and cobalt, with a crustal abundance of up to 950 ppm (*vs.* 180 and 10 ppm for Ni and Co, respectively), contributing to its cost stability and market affordability in recent years. Furthermore, the multivalent nature of manganese (Mn^{2+} to Mn^{7+}) enables the design of diverse cathode materials with tunable crystal structures.[8] Certain Mn-based frameworks exhibit high redox potentials, thereby enabling enhanced specific capacity in high energy battery applications. However, one of the biggest challenges in commercializing Mn-based cathode materials for rechargeable batteries is the dissolution-migration-deposition process, which leads to capacity decay during repeated insertion and deintercalation processes.[7,9] Such a dissolution-migration-deposition process affects the composition of the cathode electrolyte interface (CEI) layer on the cathode side due to deterioration reaction between the electrolyte and the interface.[10,11] To tackle these issues, numerous strategies have been applied to enhance reaction dynamics, inhibit the dissolution of Mn ions, and stabilize the CEI layer, which showed the great promise of Mn-based cathode materials.

Herein, we systematically examine the recent advances of Mn-based cathode materials from the perspective of energy

[a]*State Key Laboratory of Catalysis, Dalian Institute of Chemical Physics, Chinese Academy of Sciences, Dalian, China. E-mail: xiaoenw@dicp.ac.cn; zwchen@dicp.ac.cn*
[b]*School of Chemistry and Chemical Engineering, Nantong University, Nantong 226019, China. E-mail: tzyang@ntu.edu.cn*
[c]*Hubei Key Laboratory of Energy Storage and Power Battery, School of New Energy, Hubei University of Automotive Technology, Shiyan 442002, PR China*

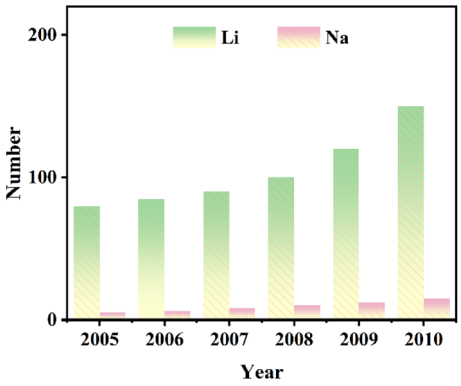

Fig. 1 Publication analysis of Mn-based cathode materials for Li/Na ion batteries from 2005 to 2025.

storage applications, with detailed discussion on their inherent limitations and ongoing challenges. We present targeted optimization strategies to address these issues, with particular emphasis on mechanistic understanding including Mn dissolution oxygen release mechanisms using advanced characterization techniques and theoretical calculations/machine learning. More importantly, for the purpose of comparison of costs, we further conducted a comprehensive comparison between Mn-based cathode materials and existing cathode materials from the perspective of life cycle assessment and techno-economic analysis. This integrated perspective bridges fundamental research with practical applications and commercialization requirements of Mn-based cathode materials, providing a roadmap for developing viable Mn-based energy storage systems.

To better reflect the development trajectory of Mn-based cathode materials, we conducted a statistical analysis of published papers related to Mn-based cathodes for LIBs and SIBs over the past two decades (2005–2025). As shown in Fig. 1, the research on Mn-based cathodes has experienced three distinct stages. From 2005 to 2010, the field was in the initial exploration phase, with a small number of publications focusing on the basic properties of classic materials such as spinel $LiMn_2O_4$. The period 2011–2020 witnessed rapid growth in research activity, attributed to the urgent need for low-cost energy storage materials and the emerging interest in SIBs, leading to extensive investigations on structural optimization and performance enhancement strategies. Since 2021, the research has entered an in-depth optimization stage, with a steady high volume of publications concentrating on solving inherent performance bottlenecks and evaluating commercialization potential. This statistical trend aligns with the content of this review, further confirming the increasing academic attention and practical value of Mn-based cathode materials (Fig. 1).

2 Mn-based cathode materials

2.1 Representative Mn-based cathode materials

Mn-based oxides demonstrate exceptional compositional flexibility, allowing for the formation of various cathode material derivatives through cation incorporation. The most technologically significant variants include spinel-type, layered-type, and olivine-type structures (Fig. 2). Each of these structures offers distinct electrochemical advantages. Due to their complementary advantages, such as structural stability in spinel Mn-based oxides, high theoretical capacity in layered Mn-based oxides, and superior theoretical energy density in olivine compounds, these three Mn-based cathode material families are considered the most promising development directions for next-generation batteries.

2.1.1 Spinel Mn-based oxides. Spinel Mn-based oxides have been widely used in lithium (Li)-ion batteries (LIBs) due to their good structural stability. They have a cubic spinel AB_2O_4 structure with the *Fdm*3 space group, where Li is located at the A position and occupies 1/8 of the tetrahedral position, Mn is in the B position and occupies 1/2 of the octahedral position, and O forms a face-centered cubic (FCC) array. Adjacent MnO_6 octahedra share edges, forming a 3D Mn_2O_4 network in which Mn has an average oxidation state of +3.5.[12] The delithiation of $LiMn_2O_4$ provides two close voltage plateaus, with a voltage of about 4 V relative to Li^+/Li. During this process, the cubic symmetry is well maintained, leading to its good structural stability. Therefore, spinel $LiMn_2O_4$ can be used as a stable, low-cost cathode for energy storage applications. However, the energy density and theoretical specific capacity of $LiMn_2O_4$ are relatively low, around 650 Wh kg^{-1} and 148 mAh g^{-1}, respectively. Another issue with $LiMn_2O_4$ is related to its poor cycling performance due to Mn dissolution at high voltages (>4.3 V) or in acidic electrolyte. The dissolution of Mn is mainly attributed to the release of Mn^{2+}, which originates from the disproportionation of Mn^{3+}. Since the low valence state of Ni^{2+} can increase the valence state of Mn, further preventing the Jahn–Teller effect and Mn dissolution, the well-known derivative $LiNi_{0.5}Mn_{1.5}O_4$ material was prepared by Ni^{2+} doping to effectively stabilize the crystal structure. $LiNi_{0.5}Mn_{1.5}O_4$ has a higher

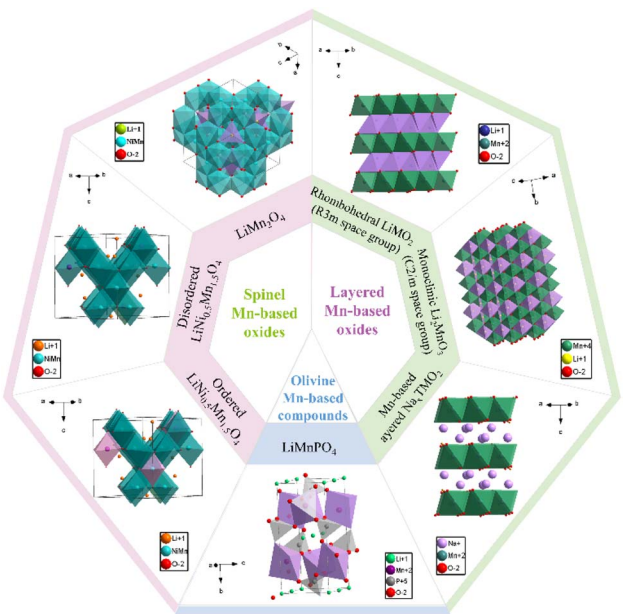

Fig. 2 A summary of the representative Mn-based cathode materials.

potential plateau of approximately 4.7 V, a higher energy density of 650 Wh kg^{-1}, and a theoretical capacity of 147 mAh g^{-1}. $LiNi_{0.5}Mn_{1.5}O_4$ is a promising high-voltage cathode material, though interfacial stability with conventional electrolytes remains a key challenge.[13] Aurbach *et al.*[14] developed two suspension electrolytes by incorporating trimesic acid (TMA) or terephthalic acid (TPA) into the conventional LP57 electrolyte (1.0 M $LiPF_6$ in EC/EMC = 3 : 7) and evaluated their performance in high-voltage $Li||LiNi_{0.5}Mn_{1.5}O_4$ cells at 30 °C. The TMA/TPA additives induce the formation of a LiF-rich solid electrolyte interphase (SEI) on the anode, which optimizes Li plating/stripping, reduces voltage hysteresis, and suppresses electrolyte decomposition during long-term cycling. Electrochemical tests confirm that the modified electrolytes significantly enhance cell cycling stability, rate capability, and capacity retention: $Li||LiNi_{0.5}Mn_{1.5}O_4$ cells with LP57 + TMA and LP57 + TPA achieve 98% and 92% capacity retention after 400 cycles, respectively, far outperforming the reference LP57 electrolyte (38% retention). Additionally, the $LiNi_{0.5}Mn_{1.5}O_4$ cathodes in the modified electrolytes exhibit superior structural, morphological, and thermal stability post-prolonged cycling. Separately, Lim *et al.*[15] optimized $LiNi_{0.5}Mn_{1.5}O_4$ synthesis *via* the Pechini sol–gel method to obtain uniform particles and precise calcination temperature control. They further employed density functional theory (DFT) calculations and electrochemical measurements to determine optimal conditions for uniform coating of the electrode surface with the oxide solid electrolyte $Li_{6.28}Al_{0.24}La_3Zr_2O_{12}$ (LALZO), aiming to improve Li^+ conductivity and enhance cycling/thermal stability. The LALZO coating physically isolates the electrode from the electrolyte, suppressing interfacial side reactions and boosting ion conductivity. Consequently, the modified electrode exhibits enhanced rate capability and significantly improved capacity retention (100 cycles at 0.2 C).

Research on $NaMn_2O_4$ began relatively late compared to $LiMn_2O_4$. $NaMn_2O_4$ was first synthesized in 2009 using a high-pressure synthesis method[16] and its electrochemical performance as a sodium (Na)-ion battery (SIB) cathode material was explored in 2014.[17,18] $NaMn_2O_4$ adopts an orthorhombic $CaFe_2O_4$-type structure with a *Pnam* space group, showing potential as high voltage cathodes with high specific capacity and stable cycle performance.[19] This spinel phase $NaMn_2O_4$ has been investigated and showed a capacity of 65 mAh g^{-1} in the voltage range of 2.0–4.0 V with a good capacity retention after 200 cycles.[19] However, $NaMn_2O_4$ still suffers from several challenges, such as insufficient air stability, rapid capacity decay due to disproportionation reactions, Mn dissolution in the electrolyte, poor thermal stability under overcharging or high-temperature conditions, and the risk of thermal runaway.

2.1.2 Layered Mn-based oxides. $LiMnO_2$ was the first developed Mn-based material.[20] As a promising cathode material for LIBs, $LiMnO_2$ has a monoclinic and a layered structure with a high theoretical capacity of 285 mAh g^{-1}.[21] This typical Li-ion layered Mn-based oxide is formed by an edge-sharing MnO_6 octahedral structure. Li-ions are located in the octahedral coordination environment of oxygen, forming the so-called O3 stacking configuration. The Li_2MnO_3 ($Li[Li_{1/3}Mn_{2/3}]O_2$) structure can be formed by increasing the Li/Mn ratio in the layered $LiMnO_2$ to improve the structural stability. In 1991, Thackeray found that $Li_{2-2x}MnO_{3-x}$ ($0 < x < 1$) showed significantly better structural stability than the layered $LiMnO_2$ cathode material, pioneering the use of Li-rich layered oxide (LLO) materials in LIBs.[22] In 1999, Kalyani discovered that Li_2MnO_3 can be activated and exhibit high capacity when the charging voltage reaches 4.5 V, sparking significant interest in this material.[23] Combined with high specific capacity (>250 mAh g^{-1}@0.1 C), low cost, and good performance, Li-rich Mn-based (LRM) layered oxide is considered as the most promising candidate material for the next generation of high-specific-energy LIBs. Li_2MnO_3 structure derives the well-known "composite structure" Li-rich Mn-based layered oxides (Mn-LLO), which provide a reversible capacity exceeding 300 mAh g^{-1}. Mn-LLO shows a characteristic two-step electrochemical reaction during the initial charging process. The cationic redox of Mn is triggered with a voltage slope below 4.4 V, whereas the anionic redox of oxygen is activated above 4.4 V, resulting in a voltage stabilization at ~4.5 V. During the initial charging-discharging process, O_2 gas is generated and released caused by the oxidation of partial active oxygen, resulting in irreversible capacity loss. When the voltage is higher than 4.5 V, irreversible oxygen release also occurs to decrease the binding energy of Mn ions and oxygen. The continuous structural transformation from the layered phase to the spinel phase results in voltage decay and poor cycling performance, and the irreversible structure transformation deteriorates the rate performance of Mn-LLO.

Different from Li-layered materials, the stacking sequence of Na-layered oxides is greatly affected by the nature of TM and composition, as well as the Na content in the alkaline layer. According to Delmas' annotation, layered SIB cathode materials can be divided into O-type and P-type.[4] In terms of the structure of layered oxide, it can be divided into the P2, O3, and P3 phases.[4] Owing to the high theoretical capacity of 243 mAh g^{-1} and low cost of Na_xMnO_2, it becomes more competitive than other Na_xMO_2 such as Na_xCoO_2. The O3 phase and P2 phase are the most common structural polymorphs of layered oxides used as SIB cathodes.[24] The O3 phase consists of alternating Na layers and Mn layers in the oxygen ion skeleton, tightly packed in an ABCABC pattern, in which Na ions and Mn ions are located at the octahedral positions of the Na layer and Mn layer, respectively. In contrast, the oxygen ion framework of the P2 phase stacks in an ABBAABBA manner, with all Na^+ located at triangular prism sites of the Na layer.[25,26] In addition to the O3 and P2 phases, the O2 phase of Na_xMnO_2 also shows certain electrochemical activity. The O_2 phase consists of zigzag layers of MnO_6 octahedra that share edges, with Na^+ located between the octahedral sites. However, the O_2 phase suffers from poor cycling performance due to structural collapse and amorphization caused by continuous strain and deformation.

The tunnel Na_xMnO_2 with an orthorhombic structure is another electrochemical active Na_xMnO_2, in which all of the Mn^{4+} ions are located at the octahedral sites (MnO_6), and Mn^{3+} ions are located at the octahedral sites and square-pyramidal sites (MnO_5) evenly. Its structure can be described as an

alternating arrangement of two types of tunnels extending along the *b*-axis with distinct cross-sectional dimensions: the larger S-type tunnels (~0.46 nm × 0.46 nm) and the smaller P-type tunnels (~0.23 nm × 0.23 nm).[27] This unique open framework not only provides abundant sites for Na^+ storage but, more critically, constructs an interconnected fast ion transport pathway. Studies have confirmed that Na^+ primarily undergoes two-dimensional diffusion with low energy barriers along the *b*-axis within the spacious S-type tunnels. This enables the material to maintain minimal structural strain even during repeated insertion/extraction of large-sized Na^+, thereby endowing it with excellent rate capability and long-term cycle stability potential.[28] Notably, $Na_{0.44}MnO_2$, a well-known tunnel Na_xMnO_2 exhibits a high theoretical capacity of 121 mAh g^{-1} and characteristic dual voltage plateaus (~3.2 V and ~4.0 V *vs.* Na/Na^+), which correspond to the two-phase reaction and single-phase reaction involved in the Na^+ extraction/insertion process, respectively.[4] As a representative tunnel-type Na_xMnO_2, $Na_{0.44}MnO_2$ exhibits excellent rate capability, which is highly desirable for practical energy storage applications. Specifically, it delivers a discharge capacity of ~200 mAh g^{-1} at 0.1 C (slow charge–discharge rate) and maintains ~110 mAh g^{-1} even at a high rate of 10 C, corresponding to a capacity retention of ~55% relative to the 0.1 C capacity.[29] This outstanding rate performance originates from its open tunnel structure, which provides unobstructed channels for rapid Na^+ intercalation/deintercalation and minimizes structural distortion during high-rate cycling. Bulk doping is one of the core approaches to stabilize the crystal structure. Introducing doped ions to partially replace Mn can not only effectively suppress the Jahn–Teller distortion, but also increase the material's average operating voltage and Na^+ diffusion coefficient, enhance structural stability, and improve cycling performance.[30] Surface modification is another key strategy. Coating a uniform carbon layer *via* a simple liquid-phase method can significantly reduce the side reactions between the electrode surface and electrolyte, effectively inhibit Mn dissolution, and thus greatly improve long-term cycling stability.[31] By continuously optimizing bulk doping, advancing interface engineering, and designing nanostructures to overcome the potential irreversible lattice phase transition during deep charging (high Na^+ extraction state) and lattice distortion induced by Mn^{3+} (a Jahn–Teller ion), the electrochemical performance of this material system—especially its cycle life—is being systematically enhanced, demonstrating great potential as a high-power, long-life cathode material for sodium-ion batteries.[32]

2.1.3 Olivine Mn-based compounds. Research on olivine Mn-based phosphate compounds was initiated after Good-enough's discovery of $LiFePO_4$ as a viable cathode material for LIBs.[33] After the discovery of $LiFePO_4$, numerous compounds belonging to the olivine type $AMPO_4$ (A = Li and Na, M = Fe, Co, Ni, and Mn) were developed to enhance cathode material performance.[34] While $LiFePO_4$ was extensively studied for its remarkable cycle life, its practical application was constrained by the modest voltage platform (~3.4 V). This limitation prompted the exploration of $LiMnPO_4$, which offers a higher operating voltage (4.1 V *vs.* $LiFePO_4$'s 3.45 V) while maintaining comparable stability, resulting in an 20% higher energy density and theoretical energy density (701 Wh kg^{-1} *vs.* 586 Wh kg^{-1}).[35]

Olivine $LiMnPO_4$ consists of a hexagonal close-packed (hcp) framework of oxygen with a *Pnma* space group, where Mn and Li occupy octahedral sites, and P occupies tetrahedral sites, respectively.[10] In contrast to $LiMnPO_4$, $NaMnPO_4$ exhibits two distinct phases including olivine and maricite. While the stable maricite $NaMnPO_4$ phase can be easily synthesized under ambient conditions, it is electrochemically inactive due to the absence of Na^+ diffusion channels in its crystal structure. Olivine $NaMnPO_4$ consists of zigzag chains of NaO_6 octahedra that share edges, which can serve as a 1D pathway channel for Na^+ diffusion.[36] in addition to being less toxic, cost-effective, and high-energy-density materials, olivine type $LiMnPO_4$ (or $NaMnPO_4$) possesses exceptional safety characteristics, originating from the strong P–O covalent bonds in their crystal structure, which stabilizes the ion extraction/inerstion processes.[37] However, lattice distortion caused by the Jahn–Teller effect leads to the poor intrinsic electronic conductivity of olivine materials with 10^{-10} to 10^{-14} S cm^{-1}. Besides, the electron and hole migration barrier of the lithiation/delithiation process is higher than that of $LiFePO_4$. Metastability of the $MnPO_4$ phase hinders the delithiation of $LiMnPO_4$, leading to $LiMnPO_4/MnPO_4$ phase mismatch.[38]

The major challenge of $NaMnPO_4$ is the low specific capacity and poor electronic conductivity, limiting their application in SIBs. Compared to $NaFePO_4$, few studies focus on the olivine $NaMnPO_4$ probably due to its poor electrochemical performance in SIBs.[35,39] Priyanka reported preparing $NaMnPO_4$ using manganese acetate as the precursor.[40] The as-prepared sample exhibited excellent performance with an initial capacity exceeding 100 mAh g^{-1} at 0.1 C, probably due to the generation of the carbon source from acetate decomposition, thereby enhancing the conductivity and porosity of $NaMnPO_4$.

$LiFe_xMn_{1-x}PO_4$ ($0.1 < x < 0.9$) is a binary olivine material between $LiMnPO_4$ and $LiFePO_4$, that combines the advantages of $LiFePO_4$ and $LiMnPO_4$. For example, Fe^{2+} doping can reduce electrochemical polarization and enhance electrode redox reversibility and ion shuttling and diffusivity capability. Meanwhile, energy density and thermal stability can be tailored by adjusting Mn content. In 1997, Mn doped $LiFePO_4$ (ref. 41) was first reported to present a dual-voltage platform (3.5 V of Fe^{3+}/Fe^{2+} and 4.1 V of Mn^{3+}/Mn^{2+}) by increasing the content of Mn. The superexchange effect of Fe^{3+}–O–Mn^{2+} reduces the redox potential of Mn^{3+}/Mn^{2+} from 4.3 V to 4.1 V, broadening the voltage window of $LiFePO_4$ to improve the energy density. Whereafter, Yamada[42] reported that excessive Mn doping ($x < 0.5$) might lead to Jahn–Teller distortion of Mn^{3+} and reduce the cycling stability. Delacourt[43] discovered through *in situ* XRD that Mn doping inhibits the decomposition of $LiFePO_4$ at high temperatures. The Mn–O bond (~402 kJ mol^{-1}) is stronger than the Fe–O bond (~372 kJ mol^{-1}); an appropriate amount of Mn ($x \sim 0.7$–0.8) can enhance lattice stability, inhibit high-temperature phase transformation, and significantly improve the thermal stability of $LiFePO_4$. Meanwhile, the Mn^{3+}/Mn^{2+} redox pair is more stable than Fe^{3+}/Fe^{2+} at high temperatures, reducing the accumulation of Fe^{3+} and thereby suppressing the

risk of oxygen release. In addition, challenges such as low electronic conductivity, poor rate performance, and Mn dissolution of $LiFe_xMn_{1-x}PO_4$ can be further modified by optimized preparation methods and the carbon coating strategy.[37,44] To address the issue of poor electrical conductivity, Liu synthesized carbon-coated $LiMn_{0.5}Fe_{0.5}PO_4$/C by the high-energy ball-milling-assisted sol–gel method.[45] The as-prepared sample exhibited an initial discharge capacity of 128.6 mAh g^{-1} and promising capacity retention of 93.5% after 100 cycles at 1 C. Similarly, Luo *et al.* developed $LiMn_{0.8}Fe_{0.2}PO_4$/C nanocrystals *via* a solvothermal method.[46] By tuning the pH value and precursor ions, the sample showed a poor Mn dissolution rate and a good electrochemical performance with a capacity of 134.6 mAh g^{-1} and capacity retention of 96.03% after 200 cycles at 1 C, with low charge transfer resistance and an excellent diffusion coefficient.

2.1.4 Other Mn-based cathode materials. Other Mn-based cathode materials such as Li_6MnO_4 (ref. 47) serve as a good LRM cathode candidate with a high theoretical capacity of 1001 mAh g^{-1}. Lee discovered the electrochemical activity of $Li_{1.211}Mo_{0.467}Cr_{0.3}O_2$ and found that the double-redox structure in Li-rich materials has the advantage of higher theoretical specific capacity (>250 mAh g^{-1});[48] research on double-redox compounds mainly focuses on Li-rich materials, such as $Li_2Mn_{2/3}Nb_{1/3}O_2F$ and $Li_2Mn_{1/2}Ti_{1/2}O_2F$ which can deliver capacities of 304 mAh g^{-1} and 321 mAh g^{-1} under cycling between 1.5 V and 5.0 V at 20 mA g^{-1}, respectively.[49] On the other hand, Na-rich Mn-based materials, such as pyrophosphate $Na_xMnP_2O_7$ are also stable SIB cathode materials, consisting of MnO_6 sites and P_2O_7 groups, which forms a framework with Na ions to allow Na ions to diffuse. Liu studied the use of $Na_2Mn_{3-x}Fe_x(P_2O_7)_2$ as the SIB cathode, and the results showed that the diffusion coefficient of Na ions increased by two orders of magnitude, and the capacity was approximately 86 mAh g^{-1}.[50] Mn-based NASICON-type $Na_4VMn(PO_4)_3$ is also considered as one of the viable candidates for Mn-based phosphate cathodes. However, the slow kinetics and negative structural degradation still limit their utilization in SIBs. To address these challenges, Xu developed an $Na_4V_{0.8}Al_{0.2}Mn(PO_4)_3$ cathode,[51] which showed good Na^+ kinetics and structural stability. The discharge capacity is 84 mAh g^{-1} and the capacity retention rate is 92% after 1000 cycles at 5 C. To further advance the development of Mn-based cathodes, combining high-throughput theoretical calculations and Mn–O phase diagrams will play an important role in exploring the structure and evaluating the properties of new Mn-based materials, especially LRM oxides with metastable structures and high capacities.

To facilitate a rapid comparison of the structural characteristics and electrochemical performances of the materials discussed above, a comprehensive summary is provided in Table 1. Despite the distinct advantages summarized in Table 1, such as the high capacity of Li-rich oxides and the fast kinetics of tunnel-type structures, Mn-based cathodes still face several critical bottlenecks that hinder their practical application. These limitations, including severe capacity fading, voltage decay, and Mn dissolution, are intrinsically linked to their crystal structures and electrochemical mechanisms. The following section (Section 2.2) will delve into the fundamental challenges associated with Mn-based cathode materials.

2.2 Challenges associated with Mn-based cathode materials

Due to the large ionic radius, special electronic configuration and redox properties of manganese, the application of Mn-based materials as cathode materials for LIBs/SIBs is usually accompanied by several critical issues, including the Jahn–Teller effect, Mn and TM ion dissolution, oxygen release at high voltage, and air instability of layered oxides.

2.2.1 Jahn–Teller effect. The Jahn–Teller effect of Mn is recognized as one of the biggest challenges in Mn-based cathode materials for LIBs/SIBs. In 1937, H.A. Jahn and E. Teller first proposed that a non-linear molecule system in a degenerate energy state shows lower stability when the nuclei are in a symmetrical configuration.[52] The system undergoes spontaneous symmetry breaking to eliminate its degeneracy, resulting in a stabilized configuration with reduced energy.

When the high-spin Mn^{3+} cation ($t_{2g}^3e_{1g}$) is located at the center of the MnO_6 octahedron, a single e_g electron occupies the e_g orbital (e_{1g}), resulting in the asymmetric occupation of the e_g orbital. As a result, the entire d orbital becomes incompatible with the O_h symmetry of the regular octahedron, resulting in the distortion of the Mn–O bond and the reduction of the symmetry of MnO_6 from O_h to D_{4h} (Fig. 3a). In contrast, Mn^{2+} and Mn^{4+} configurations maintain symmetric electron occupation states of e_g orbitals. Therefore, only high-spin Mn^{3+} exhibits Jahn–Teller activity, unlike the symmetric configuration high-spin Mn^{2+} and Mn^{4+}. Compared to other TM cations, Co and Ni are typically Jahn–Teller inactive, which can be attributed to the jagged Jahn–Teller ordering of the TMO_2 plate along the elongated axis or the absence of electrons in orbitals. The strong Jahn–Teller effect caused by the high spin Mn^{3+} present in Mn-based materials reduces the stability of its electronic structure, leading to spontaneous structural distortion and disproportionation reactions. At the same time, the Jahn–Teller effect induces Mn dissolution and oxygen release, ultimately reducing its specific capacity and cycling stability. In recent years, researchers found that introducing different ligands to construct low-spin Mn^{3+} complexes, along with customizing the redox valence state of Mn effectively mitigates the Jahn–Teller distortions, enhancing the stability of Mn-based materials. It has been proved that microstructure design also can suppress the Jahn–Teller effects. Interface orbital sorting, vertical interfacial orbital sorting of the dz^2 orbitals of spinels, and layered crystal domains may destroy long-range orbital sorting, thereby significantly reducing the Jahn–Teller effect. It is generally believed that the Mn^{3+} disproportionation reaction caused by the Jahn–Teller effect mainly leads to Mn dissolution and the main dissolved ions are found to be Mn^{2+} species. In addition, the electrochemical cycling, and protonation process also cause Mn dissolution, which can be accelerated by high temperature and surface area exposure.

A further issue triggered by the Jahn–Teller effect is oxygen release. Oxygen atoms can easily escape from the crystal lattice of manganese-based cathode materials, causing structural

Table 1 Comparative summary of key properties of typical Mn-based cathode materials for LIBs and SIBs

Material type	Crystal structure	Battery system	Key performance indicators	Typical modification strategies
$LiMnO_2$	Monoclinic layered, O3 stacking	LIBs	Theoretical capacity: 285 mAh g^{-1}; a ctual capacity (~0.1 C): ~ 150–180 mAh g^{-1}; p oor cycling stability due to structural distortion	Increasing the Li/Mn ratio to form Li_2MnO_3; cation doping (*e.g.*, Al^{3+} and Co^{3+}) to suppress Jahn–Teller distortion
Li-rich Mn-based layered oxides (LLOs)	Layered "composite structure", O3 stacking	LIBs	Theoretical capacity: >300 mAh g^{-1}; a ctual capacity (~0.1 C): >250 mAh g^{-1}; d ual voltage plateaus (~3.2 V and ~4.5 V); v oltage decay and irreversible oxygen release	Cation doping (Ni^{2+} and Co^{2+}); o xygen redox regulation; i nterface engineering (surface coating with Al_2O_3)
Spinel $LiMn_2O_4$	Spinel framework (*Fd*-3*m* space group)	LIBs	Theoretical capacity: 148 mAh g^{-1}; a ctual capacity (~0.1 C): ~ 120–130 mAh g^{-1}; m oderate rate capability; c apacity fading at elevated temperatures	Surface coating (carbon and $LiNiPO_4$); p artial substitution of Mn (*e.g.*, $LiMn_{1.5}Ni_{0.5}O_4$)
Layered Na_xMnO_2 (O3 phase)	Layered, ABCABC oxygen stacking, Na^+ at octahedral sites	SIBs	Theoretical capacity: 243 mAh g^{-1}; a ctual capacity (~0.1 C): ~ 180–200 mAh g^{-1}; p oor cycling stability due to phase transition	Phase regulation (conversion to the P2 phase); surface modification with a carbon layer
Layered Na_xMnO_2 (P2 phase)	Layered, ABBA oxygen stacking, Na^+ at triangular prism sites	SIBs	Theoretical capacity: ~ 200 mAh g^{-1}; a ctual capacity (~0.1 C): ~ 160–180 mAh g^{-1}; b etter structural stability than the O3 phase	Cation doping (Mg^{2+} and Zn^{2+}); e lectrolyte optimization to reduce side reactions
Tunnel-type $Na_{0.44}MnO_2$	Orthorhombic, 3 × 3 tunnel framework (S-type/P-type tunnels)	SIBs	Theoretical capacity: 121 mAh g^{-1}; a ctual capacity (~0.1 C): ~ 115–120 mAh g^{-1}; r ate capability (~10 C): ~ 75 mAh g^{-1} (62.5% retention); d ual voltage plateaus (~3.2 V and ~4.0 V)	Bulk doping (*e.g.*, Ti^{4+} and Fe^{3+}); s urface coating ($NaTi_2(PO_4)_3$ and carbon layer); n anostructure design

degradation, especially under additional stimuli such as thermal runaway and collisions. The release of highly oxidizing oxygen species degrades the electrolyte components and deteriorates the cathode electrolyte interface (CEI), thereby accelerating the structural degradation of the cathode material. In addition, the released oxygen forms O_2 gas or oxidizes the electrolyte to form CO_2, causing battery expansion and failure. These exothermic processes can trigger thermal runaway, which further accumulate oxygen release and structural degradation, leading to serious safety issues. For spinel $LiMn_2O_4$, it undergoes a disproportionation reaction from Mn^{3+} to Mn^{2+} and Mn^{4+} at high voltage charging, which is normally accompanied by an irreversible phase change to produce electrochemically inactive Mn_3O_4 and $Li_4Mn_5O_{12}$. The existence of the Mn_3O_4 phase will lead to the formation of soluble Mn^{2+} ions and the release of oxygen.[53]

During the discharge process, a large number of defects in the interface after the TM dissolves lead to uneven diffusion of Li ions, triggering the generation of $Li_2Mn_2O_4$. During this phase change process, the unit cell volume of the material increases irreversibly, which results in accelerating the dissolution of the TM. For Mn-LLO, Cao reported that in $Li_{1.2}Ni_{0.13}Co_{0.13}Mn_{0.54}O_2$, during low-rate cycling, gradient TM dissolution destroyed the mechanical integrity of the secondary particles, causing the internal TMs to dissolve gradually.[54] Simultaneously, irreversible layered-to-spinel phase transformation occurs and then leads to the decay of capacity and average voltage. During high-rate cycling, TM dissolution

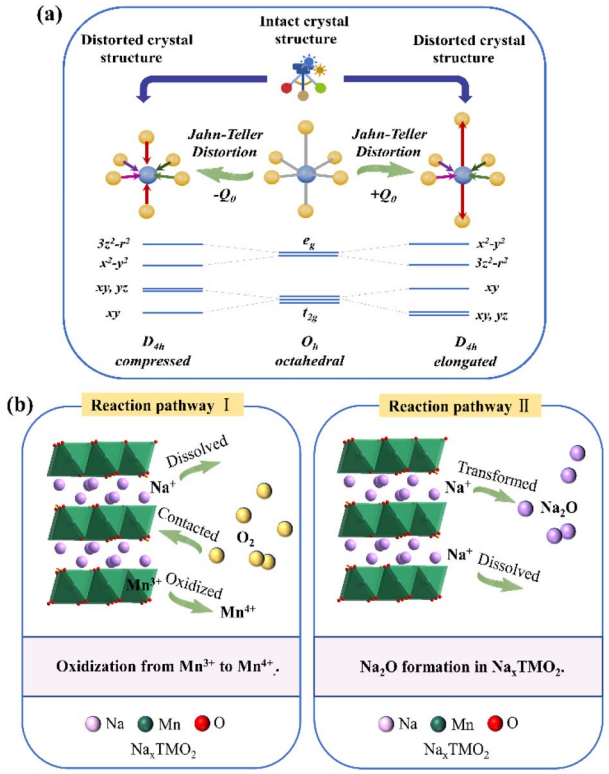

Fig. 3 (a) Schematic diagram of the Jahn–Teller effect. (b) Two major redox reaction pathways involved in Na dissolution.

primarily occurs at the particle surface, inducing a layered to rock-salt phase transition, which ultimately causes more severe capacity decay than that observed under low-rate cycling conditions.

2.2.2 Structural instability in moist air. The high reactivity of Mn-based materials with CO_2 and H_2O in the external environment, forming Li-containing surface compounds, poses an additional major challenge. The highly oxidizing TM ions would catalyze electrolyte decomposition in the charging state, which will accelerate the electrolyte consumption and generate a thick solid electrolyte interface layer on the electrode material surface. To obtain ordered layered Mn-based materials, excessive Li sources are often added during the preparation of mixed Li sintering, which leads to the existence of Li residues on the surface of the materials. The residue would react with H_2O and CO_2 in air to generate Li_2CO_3 and LiOH. In particular, due to the nature of the layered structure with large Na-ions, both CO_2 and moisture can lead to deterioration of cathode materials even after a few hours of exposure to air which leads to a loss of structural and chemical integrity. Critical issues such as degradation caused by humid environments pose great challenges to the long-term storage and practical application of SIBs.

During the degradation process caused by air contact, alkaline and hygroscopic compounds such as sodium hydroxide, sodium carbonate, and sodium bicarbonate[55] are formed on the particle surface by the reaction of lattice Na^+ and CO_2 in air, and the formation water molecules is accelerated through Na^+/H^+ exchange. The Na^+ is dissolved from the crystal lattice, ultimately leading to the formation of a hydrated phase or structural transformation. In addition, the formation of alkaline compounds can also cause particle aggregation, affecting the uniformity of the slurry during electrode preparation. The residual alkaline compounds on the particle surface increase the resistance of the cathode material and hinder the diffusion of Na^+ and electrons. In addition, studies have shown that sodium carbonate electrochemically decomposes at around ~4 V and releases CO_2 gas, further reducing the stability of the electrode. Two major redox reaction pathways involved in Na dissolution have been summarized, as shown in Fig. 3b. (1) Oxygen in air converts Mn^{3+} to Mn^{4+}, resulting in further loss of Na^+ to balance the charge, thus forming more Na-deficient materials. (2) Na oxide is formed as an intermediate to maintain charge balance. In both reaction pathways, Na_xTMO_2 exhibits reducing behavior due to its low open-circuit voltage (OCV), which is thermodynamically favorable for initiating redox processes under ambient storage conditions.

By leveraging theoretical calculations to direct the doping or coating design strategies for layered oxides, there is a promising prospect of augmenting their stability in humid air, bolstering safety levels, and preserving the battery cycling performance. To understand the degradation mechanism of O3 layered oxides in ambient air, Li calculated the first-principles reaction energy through density functional theory (DFT) based on the model structure of O3 with the chemical formula $NaCo_{1-x}M_xO_2$,[56] where M represents a commonly used dopant, one of the 15 metals, namely Li, Mg, Al, Ca, Ti, V, Cr, Mn, Fe, Co, Ni, Cu, Zn, Zr, and Nb. To have a better understanding of the correlation, two structural properties, V (unit cell volume of the doped structure), and d_{OH} (O–H bond length of the inserted H_2O molecule) were combined to generate a new descriptor, d_{OH}^2/V, successfully evaluating the air stability of each doped material. Elements such as Al, Li, Cu, Fe, and Mg, are often called effective dopants for improving air stability, while Mn-based materials are less stable and expensive dopants such as Nb and Zr are even worse, and Ca and Ti are less efficient dopants.

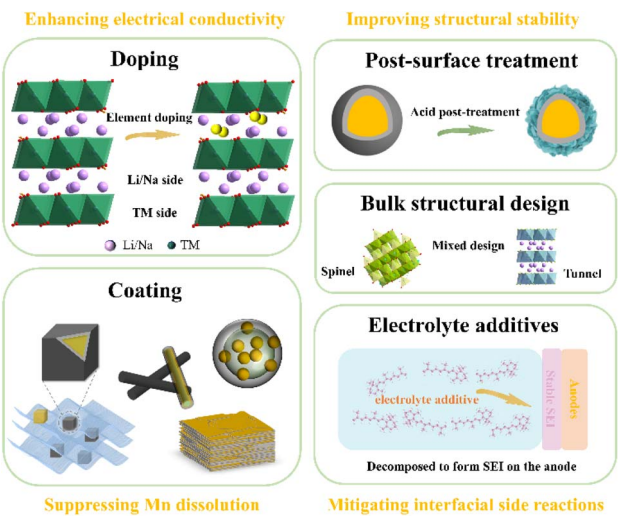

Fig. 4 Representative modification strategies for Mn-based materials.

Hydrophobic coating treatments can be used to repel water and moisture and direct contact with air or moisture can be prevented by applying a physical protective layer (such as metal oxide or phosphate). Both coating designs mitigate the degradation of cathode materials in air.

3 Optimization strategies for Mn-based cathode materials

With high specific discharge capacity and energy density, manganese-based cathode materials show huge application prospects. However, several intrinsic drawbacks significantly impede their practical implementation, such as low initial coulomb efficiency (ICE), poor rate performance, serious voltage dropping, and gas generation during charge and discharge cycling, which seriously affect the commercial application of Mn-based materials in LIBs or SIBs. To tackle the above-mentioned challenges, various modification strategies (Fig. 4) have been proposed to enhance the performance of Mn-based materials in LIBs/SIBs, such as doping, surface coating, liquid/gas phase post-treatment, new structural construction, and electrolyte additive incorporation, among which element doping and surface coating have been widely adopted as the most effective approaches.

3.1 Element doping

Elemental doping can improve cathode material performance by enhancing the charge transfer and the structure stability through several mechansims: strengthening oxygen binding energy to mitigate oxygen loss, as well as boosting both ionic and electronic conductivity. According to the charge properties, element doping can be divided into cation doping and anion doping. In terms of the doping sites, they can be roughly divided into the following three categories: (1) the doping of Li/Na sites, such as K[57,58] and Ti;[59] (2) the doping of TM sites, such as Zr,[60,61] Nb,[62–66] Ta,[67] Al,[68,69] Cr,[70] Mg[71] and Ti;[72] (3) the doping of O sites, such as F[49,58,73] and S.[74]

Since the alkali metal elements K and Li/Na belong to the same main group, they have similar electronic structures and electrochemical properties. Na and K were usually used for doping modification of Mn-based LIBs in the early days. Park[75] studied the effect of doping with different Na contents on the performance of $Li_{1.167-x}Na_xNi_{0.18}Mn_{0.548}Co_{0.105}O_2$ ($0 \geq x \geq 0.1$) and found that when $x = 0.05$, the diffusion coefficient of a Li-ion increased from 1.35×10^{-9} cm^2 s^{-1} to 3.34×10^{-9} cm^2 s^{-1}, the capacity retention rate increased from 83% to 92%, and the rate capability was also improved from 189 to 208 mAh g^{-1} at a high current density of 1.0 C. Li obtained the sample K^+ doped $Li_{1.2}Mn_{0.54}Co_{0.13}Ni_{0.13}O_2$ using α-MnO_2 containing the K element as the raw material *via* the *in situ* synthesis and performed systematic research on the effect of the K element,[57] and found that K^+ with a larger radius could reduce the generation of Li vacancies and migration of manganese, and hinder the formation of the spinel phase structure. This material presented good cycling stability with a capacity retention of 85% (initial capacity of 315 mAh g^{-1}) at a current density of 20 mA g^{-1} after 110 cycles. Recently, Liu[59] reported a $Li_{1.2}Ti_{0.26}Ni_{0.18}Co_{0.18}Mn_{0.18}O_2$ cathode material and designed a structure with Ti^{4+} ions occupying the Li layer, different from the conventional TM layer doped with Ti^{4+} ions. Electron energy loss spectrum (EELS) analysis indicated that the Ti ions were successfully doped into the Li layer and TM layer. The potential dropping of the $Li_{1.2}Ti_{0.26}Ni_{0.18}Co_{0.18}Mn_{0.18}O_2$ material is only 90 mV after 100 cycles, and the capacity retention of the $Li_{1.2}Ti_{0.26}Ni_{0.18}Co_{0.18}Mn_{0.18}O_2$ material is 97% after 182 cycles. The enhanced structural stability can be attributed to the strong ionic Ti–O bonds that strengthen the O–TM(Li)–O slabs and suppress undesirable structure transformation and mitigate the migration of TM ions during the delithiation process. Extended X-ray absorption fine structure (EXAFS) analysis shows that the peak of the Mn_2O bond becomes weaker while charging to 4.43 V, indicating the change in the Mn_2O bond length due to oxygen oxidation when Li is extracted from the TM layer. It is noted that the EXAFS spectrum of Mn recovers after discharging. TM element doping into the TM sites also led to improvement in the electrochemical performance of the Mn-based cathode materials. It was found that in $Li_{1.2}Ni_{0.16}Mn_{0.51}Al_{0.05}Co_{0.08}O_2$ (ref. 68) and trace Mg-doped $Li_{0.2}Ni_{0.13}Co_{0.13}Mn_{0.54}O_2$ (ref. 71) materials, the doping of Al and Mg at the TM site can inhibit the migration of cations and the direction of the layered structure. The transformation of the spinel structure contributes to the stability of the layered structure, reduces the cyclic voltage drop of the material, and improves the capacity and long-term cycling stability. However, since the ionic radius and metallicity of Mg are slightly different from that of Al, Al doping will not affect the change in the oxygen activation plateau during the first charge. Compared with Al doping, the stronger Mg–O bond produced by Mg doping can shorten this plateau, thereby inhibiting irreversible structural phase transitions. Zr doping has also been proven to effectively improve capacity and cycle performance. Wang[60] designed a 3% Zr doping Mn-based LLO cathode material with the chemical formula $Li_{1.2}Mn_{0.54}Co_{0.13}Ni_{0.13}O_2$ by a sol–gel method, aiming to address the oxygen-releasing issue during long-term cycling. High-angle annular dark field (HAADF) characterization shows that in the LLO-Zr sample after cycling, the particles remain stable and intact and virtually free of cracks and voids, except a ~2 nm thick spinel structure on the surface. In contrast, many intragranular voids and a thick layer of spinel and rock salt-like structures (about 8 nm) were found in the LLO sample, which was caused by the release of oxygen during the cycling process. Subsequent EELS spectral analysis further confirmed the effectiveness of Zr doping in mitigating oxygen loss. The full-cell test result shows that the long-term cycle performance of LLO-Zr after 100 cycles is higher than that of LLO at various current densities, from 0.2 to 1 C. The capacity of LLO-Zr can reach 223 mAh g^{-1} at 1 C, and the capacity retention rate after 300 cycles is 88%, while the capacity retention rate of LLO is 74%. Electrochemical impedance spectroscopy (EIS) studies have also confirmed that LLO-Zr has better rate capacity than LLO. LLO-Zr has lower resistance, which means it has faster electron and ion migration, indicating the Li^+ diffusion kinetics in LLO-Zr is faster than that in LLO. The above electrochemical

results indicate that LLO-Zr has superior electrochemical properties compared to pure LLO, including higher initial discharge capacity, better rate performance, and long-term cycling stability. DFT study results show that the oxygen vacancy formation energy of LLO after Zr doping increases, indicating that Zr doping can slow down the oxygen loss during charge and discharge cycles and enhance the stability of oxygen in the material. In addition, Zr-doped LLO shows a lower Li ion migration energy barrier, which is beneficial in improving its Li-ion diffusion performance during battery charging and discharging. Owing to the significant enhancement of the Zr–O bond strength, the incorporation of Zr into the LLO lattice greatly reduces oxygen loss. Similarly, the dissociation energy of Nb–O is 679 kJ mol^{-1}, greater than that of Mn–O (481 kJ mol^{-1}).[63] Nb doping can also form stable Nb–O bonds to reduce oxygen loss, thereby enhancing structural stability and increasing the specific capacity and voltage retention rate. Nb doping also plays an important role in improving O-type[65] and P-type[66] Mn-based cathode materials for SIBs. Nb^{5+} doping increases the lattice spacing, reduces the valence state of Mn, increases the conductivity of the material, stabilizes the layered structure of the oxide, and effectively inhibits the phase change process of the layered oxide during charging and discharging (O3 to P3, and P2 to O2). Substituting the oxygen ions with other anions is another widely used approach to strength the weak TM–O bonds. So far, it has been found that anion element (such as S^{2-} and F^{-}) doping can stabilize the layered structural framework, mitigate voltage fade, and improve the safety/cycling stability of Mn-based cathode materials. Co-doping anions with other metal elements (such as Cd/S,[76] K/F,[58] Nb/F,[49] and Ti/F[49]) can combine the advantages of each element in surface modification, the strategy of which has become a research hotspot in recent years. Recently, researchers found that F doping of the O-site is an effective improvement strategy to improve the rate and cycle performance of LRM materials. Lee's group[49] prepared two disordered-rock-salt LRM cathodes, $Li_2Mn_{2/3}Nb_{1/3}O_2F$ and $Li_2Mn_{1/2}Ti_{1/2}O_2F$, *via* a mechanochemical ball-milling method. Energy dispersive spectroscopy (EDS) was conducted to confirm the uniform dopant distribution of Nb and F on the cathodes. The prepared cathodes show high capacity and energy density when cycled between 1.5 V and 5.0 V at 20 mA g^{-1}, and $Li_2Mn_{2/3}Nb_{1/3}O_2F$ exhibits a reversible capacity of 304 mAh g^{-1} and energy density of 945 Wh kg^{-1}. Similarly, $Li_2Mn_{1/2}Ti_{1/2}O_2F$ also yields promising capacity (321 mAh g^{-1}) and energy density (932 Wh kg^{-1}). The metal oxidation and oxygen redox behaviors were confirmed by X-ray absorption spectroscopy (XAS) analysis. The high-valent cation (Nb^{5+} and Ti^{4+}) and F co-doping strategy play a crucial part in introducing Mn^{2+}/Mn^{4+} double redox. Furthermore, DFT studies suggested that, at a given delithiation level, F doping of the O site is beneficial in lowering the Mn oxidation state, thereby resulting in more redox overlap with O. Within the Mn^{2+}/Mn^{4+} redox, structural degradation was achieved to enhance the electrochemical performance.

Doping modification is a facile strategy that can effectively improve the electrochemical performance of Mn-based cathode materials. When low-valent elements are doped at the Li or Na positions, the interlayer distance of Li can be increased, facilitating the deintercalation of Li ions. In contrast, doping high-valent elements at these positions serves to reinforce the Mn–O bond and hinder the conversion of the layered structure into the spinel phase. Cation doping at TM sites is effective in augmenting the bonding energy between the dopant and oxygen, curbing oxygen loss and thus stabilizing the material structure. Moreover, anion doping at the O site plays a significant role in reducing the loss of lattice oxygen and diminishing the internal resistance of the material.

3.2 Surface coating

Surface coating is a widely used modifying approach to construct a uniform functional layer on the active material surface that can avoid direct contact with the electrolyte, thereby improving conductivity and hydrophobicity and inhibiting the continued growth of the CEI during cycling, enhancing cycle stability and ensuring good rate performance. To date, ball milling, the sol–gel method, the solvothermal method, chemical vapor deposition (CVD) and atomic layer deposition (ALD) technologies have been reported in the research on modification of Mn-based cathode materials for ultra-thin, uniform, and strong coatings.[77]

Compared to the wet chemical methods along with the complex nucleation and growth processes, ALD is a highly reliable method that can achieve continuous deposition of uniform coatings with sub-nanometer thickness accuracy on material substrates and effectively prevent various side reactions. The approach is responsive and easy to scale to meet growing demands. It is also possible to create highly controllable composite coatings by alternating different precursors. Metal oxides (such as Al_2O_3,[78–80] MgO,[81] ZnO,[82] CeO_2 (ref. 83) and TiO_2 (ref. 84)), carbon materials,[85,86] phosphates (Li_3PO_4 (ref. 87) and $AlPO_4$ (ref. 88)), AlF_3 (ref. 89) polymers,[90] and fast ionic conductors(Li_2TiO_3,[91] $La_{0.8}Sr_{0.2}MnO_{3-y}$[92] and Li_2ZrO_3 (ref. 93)) have been widely used as the surface coating materials. Among metal oxides, Al_2O_3-coated Mn-based cathodes exhibit superior cycle stability, leading to their widespread adoption in Mn-based electrode materials for LIBs and SIBs. Al_2O_3 is usually coated on the surface of the material using the ALD approach. Al_2O_3 surface modification plays an important role in inhibiting CEI reactions, side reactions between the cathode and the electrolyte during battery cycling, and layered-to-spinel phase transformation, which has been widely utilized in the preparation of high-performance and long-cycling stability LIBs.[94–96] Deng[88] found that $AlPO_4$ coating is expected to improve the reliability and electrochemical performance of spinel $LiNi_{0.5}Mn_{1.5}O_4$ cathodes at high voltages compared with Al_2O_3 coating. The discharging capacity of $AlPO_4$-coated sample shows an improved performance with the C rate increasing from 0.1 C to 5.0 C and then back to 0.1 C with higher capacity and excellent reversibility. In addition, the electrode maintained a long and stable cycle life after 350 cycles, with a high reversible capacity of 75.3 mAh g^{-1} and a capacity retention rate as high as 74.9%. The capacity fade per cycle is only 0.07 mAh g^{-1}. However, the capacity decay of pristine is 0.18 mAh g^{-1} per cycle, which is 2.6

times higher than that of the $AlPO_4$-coated sample. X-ray absorption near-edge structure (XANES) spectroscopy research further confirmed that $AlPO_4$ coating can maintain the same Mn^{4+} (MnO_2) characteristics, indicating that the ALD coating process does not change the valence state of Mn on the $LiNi_{0.5}Mn_{1.5}O_4$ surface. After charge–discharge cycles, the pristine sample shows a high proportion of Mn^{2+} peaks, indicating that the surface structure has been destroyed after cycling. In contrast, the $AlPO_4$-coated sample still mainly maintains Mn^{4+} characteristics after cycling, which means that the ALD coating effectively suppresses the precipitation of Mn^{2+}. After cycling, the element Mn may be dissolved and the structure of the pristine sample is destroyed without any surface protection. Vanaphuti[89] synthesized a Mn-LLO *via* a wet chemical method and then coated AlF_3 by the ALD technique to prepare an $Na_{0.05}Li_{1.15}Mn_{0.54}Ni_{0.13}Co_{0.13}F_{0.01}O_{1.99}$ cathode. Scanning transmission electron microscopy (STEM)-EDS depicted the presence of AlF_3 coatings with 250 nm thickness and the element distribution from the surface to the bulk. For rate performance, the 1.0 wt% AlF_3 coating provides an additional capacity of ~5 mAh g^{-1} at high rates, which is higher than that of pristine and co-doping samples. Compared with uncoated and over-coated materials, 1 wt% AlF_3 is the optimal coating amount, which exhibits better cycle stability and a smaller voltage drop. In contrast, over-coating thickness will increase the resistivity of ion transport. For cycling stability, after 150 cycles at 0.5 C, the sample with 1.0 wt% AlF_3 coating is significantly improved compared to the other sample. Further spectral characterization indicated that the coating mainly affects the Co distribution and allows Co to accumulate on the particle surface and form $Li_x(CoAl)O_y$, which is more stable than $LiTMO_2$ and $LiAlO_2$ compounds and does not undergo Li and O migration, thus leading to excellent cycling retention ability.

Carbon coating is a commonly used strategy in Mn-based cathode materials with the following advantages. (1) Uniform carbon coating can prevent particle growth and inhibit particle agglomeration, thereby reducing the Li^+ transmission distance and improving ionic conductivity. (2) A carbon coating can be treated as a protective layer and reducing agent to prevent Mn dissolution and inhibit the oxidation of Fe. (3) The carbon coating provides a pathway for electron transmission, which can tailor the surface between particles and electrolytes, and then improve electronic conductivity. The conductivity of the sample cannot be maximized with too low carbon content. In contrast, the tap density of the material will be reduced while the carbon content is too high. At the same time, an excessively thick carbon layer will affect the penetration of Li^+ and reduce the conductivity of the sample. Therefore, it is required to balance the conductivity and tap density by tailoring the thickness of the carbon coating layer. Li[85] synthesized $LiMn_{0.6}Fe_{0.4}PO_4$/carbon aerogel microspheres. Microspheres with a three-dimensional porous conductive network possess an excellent electronic conductivity of 8.5×10^{-2} S m^{-1}. Using a carbon aerogel as a carbon coating can overcome the drawback of low tap density in traditional carbon coating processes. The electrochemical results indicated that $LiMn_{0.6}Fe_{0.4}PO_4$ with a 10% carbon aerogel exhibits a superior electrochemical performance, with a 0.2 C discharge capacity of 159.1 mAh g^{-1} after 500 cycles and a 1 C rate capacity retention of 96.9%. In addition, the large specific surface area of the carbon coating will promote the side reactions between the electrolyte and the particles and induce the dissolution of Mn^{3+}. Therefore, highly graphitized carbon sources such as graphene and carbon nanotubes are commonly used in carbon coating strategies. Furthermore, a carbon material doped with heteroatoms such as N[86] and F[97] as coating materials can effectively promote surface modification. N-functionalized carbon materials have been reported to effectively improve the charge transfer reaction kinetics and inhibit oxygen release to stabilize the cycling performance. The N-doped graphene-coated $Li_{1.2}Mn_{0.6}Ni_{0.2}O_2$ cathode material exhibits a high specific capacity of 286 mAh g^{-1} at 0.2 C and maintains a capacity retention rate of 86% after 200 cycles, exhibiting slight voltage decay and high capacity retention.[86] The excellent electrochemical performance is attributed to the porous structure with high conductivity and the N-functional groups (pyridine and pyrrole), which reduces polarization and suppresses electrolyte decomposition, respectively. Surface modification of F-doped carbon in LLO forms strong Mn–F bonds,[97] which leads to the strong electronic coupling between LLO and the carbon coating, thereby enhancing the structural stability and electrochemical performance.

In addition, certain double-layer coating materials, such as $Al_2O_3/AlPO_4$,[98] can effectively promote electronic conduction and ion conduction, and inhibit the formation of the CEI layer, thereby improving cycle stability. However, they typically exhibit inferior rate capability compared with single layer coatings. Although surface coatings can partially improve the electrochemical performance of Li-rich Mn-based materials, most fail to fundamentally suppress the structural degradation. In contrast, fast ion conductor coatings not only improve the diffusion rate of Li^+ and the stability of the material, but also address the structural transformation issue. For instance, $La_{0.8}Sr_{0.2}MnO_{3-y}$ significantly enhances the electrochemical properties of LRM materials while effectively mitigating structural transformation at its root. Hu[92] reported a $La_{0.8}Sr_{0.2}MnO_{3-y}$ (LSM) coated $Li_{1.2}Ni_{0.13}Co_{0.13}Mn_{0.54}O_2$ (LM) material. The LSM coating forms a heterostructure with the LLO block,

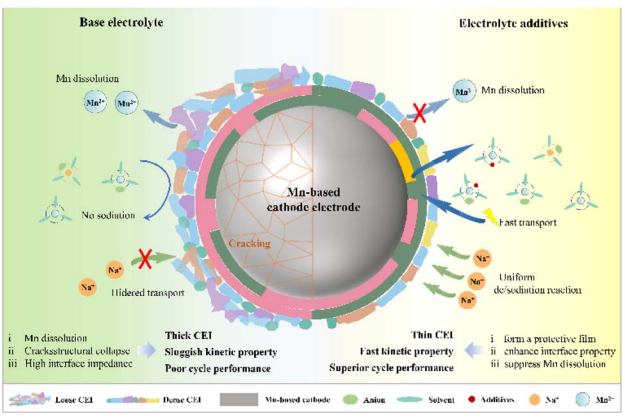

Fig. 5 The working mechanism of the electrolyte additives.

forming strong Mn–O–M bonds which can suppress oxygen release during charging. Consequently, the formation of defects and nanopores, which degrade electrochemical performance, is effectively prevented. Similar to other coatings, X-ray photoelectron spectroscopy (XPS) analysis indicated that, compared with pristine samples, LSM-coated samples have a higher level of oxygen surface redox reactions, thus suppressing voltage fading. The LSM-coating inhibits the surface electrolyte decomposition and reduces the Mn valence state and mitigates Mn dissolution, thereby preventing the layered-to-spinel transformation.

Coatings prepared through various deposition methods show their unique effects in suppressing Mn dissolution and suppressing oxygen release of Mn-based cathode materials. These variations primarily stem from differences in the coating structure and properties, which are intrinsically linked to three key factors: thickness, uniformity, and synthesis process parameters. Given the significant influence of these factors on coating performance, further optimization and precise control of deposition techniques remain critical for practical applications.

3.3 Electrolyte additives

The optimization of the electrolyte formulation is crucial for improving cathode performance, among which the use of electrolyte additives represents the most feasible strategy to enhance the electrochemical stability of Mn-based cathode materials. These additives can form protection layers on the electrode surface or modify the electrolyte properties, thereby optimizing the overall electrochemical environment.[99] The function of the electrolyte additives is to form a protective film, enhance the interface performance and suppress the dissolution of Mn, and their working mechanism is illustrated in Fig. 5. During cycling, the *in situ* formation of a dense protective film derived from electrolyte additives effectively passivates the Mn-based cathode surface.[100] This protective film inhibits electrolyte decomposition by blocking solvent penetration and Li^+/Na^+-induced side reactions, thereby stabilizing the electrode–electrolyte interface. Furthermore, additives enhance the Mn-based cathode/electrolyte interface stability by lowering interfacial resistance to accelerate Li^+/Na^+ kinetics, mitigating charge accumulation and polarization.[101] This dual effect improves cycling reversibility and overall electrochemical stability. Additionally, Mn-based cathode materials experience manganese ion dissolution during battery cycling, which compromises their structural integrity and electrochemical performance. Electrolyte additives effectively mitigate this issue through dual protection mechanisms. They form stable complexes with Mn^{2+} ions in solution, while generating a protective surface layer that physically inhibits Mn dissolution.[102] These synergistic effects significantly enhance both the structural and electrochemical stability of the cathode material.

By tailoring the additive composition and concentration, one can achieve improved cycling stability, rate capability, and coulombic efficiency.[103] Adding additives to the electrolyte can also solve the problems of TM migration and oxygen release caused by high charging voltage (4.8 V).[104] For example, Zheng[105] used a phenyl vinyl sulfone additive as a protective agent, which can form a protective CEI on the surface of the positive electrode to stabilize battery cycling. Commonly used carbonate electrolytes suffer from poor cycling stability due to the release of oxygen radicals. Many electrolyte additives, such as β-carotene,[106] trimethyl phosphate,[107] and trimethylsilyl borate[108] can capture and then eliminate the oxygen molecules, thereby enhancing the cycling stability of the material. Among them, phosphorus-containing additives can undergo chemical reactions on the surface of cathode materials to form a phosphate protective film with good electrical conductivity and stability.[109] This strategy not only prevents the side reactions between the cathode material and the electrolyte, but also improves the structural stability of the material, thereby enhancing its electrochemical performance. Adding fluorine-containing additives[110] such as $LiPF_6$ and $LiBF_4$ to the electrolyte forms a protective LiF rich film on the surface of the Mn-based cathode material. This protective film can effectively inhibit the erosion of the cathode material by the electrolyte, and at the same time increase the ionic conductivity of the material, thereby enhancing its electrochemical stability.[111] Meanwhile, nitrogen-containing additives[112] such as pyrrole, pyridine and other nitrogen-containing organic compounds can reduce the electron cloud density on the surface of Mn-based cathode materials through coordination with the active sites on the surface of the materials, thereby inhibiting the structural changes in the materials during charging and discharging and improving their electrochemical stability.[113]

At present, most of the research on the high-voltage performance of ether-based electrolytes focuses on functional additives.[114] Introducing functional additives to construct a robust inorganic component-rich CEI can effectively inhibit the decomposition of ethers at the interface.[115] Some typical additives, such as sodium difluorophosphate (NaDFP),[116] sodium difluoro-oxalate borate (NaDFOB),[117] and fluorinated ethylene carbonate (FEC),[118] are included. The solvation structure of ether-based electrolyte can be optimized by adjusting the Na salt and solvent.[119] Adjusting the concentration and type of Na salt can reduce the proportion of free ether solvent, thereby constructing a CEI mainly composed of the decomposition products of Na salt.[120] In addition, the introduction of electron-withdrawing groups can enhance the solvation structure and improve the oxidation stability of the electrolyte.[121] Although adding fluorine-substituted groups to the ether molecular structure can enhance oxidation stability,[114] this strategy significantly increases the cost of the electrolyte and is therefore not suitable for large-scale application.

In addition to the various side reactions existing in the electrolyte system that would cause battery degradation, the HF, a decomposition product of electrolyte will induce the dissolution of the Mn element as well, resulting in a capacity decrease of the cathode material. It was found that LiBOB[122] and trimethylsilyl phosphite[123] can be used as additives to eliminate the decomposition product HF of the electrolyte and improve the cycle performance of the battery. These findings highlight the critical role of additive design in mitigating Mn dissolution

and offer promising strategies for developing high-performance Mn-based cathodes in LIBs/SIBs.

3.4 Other strategies

Other modification strategies, including post-surface treatments and bulk structural designs, also significantly improve performance and safety. Gas or acid post-treatment has been extensively employed in structure control or oxygen vacancy design to promote Li^+ diffusion, suppress the voltage drop, and improve both capacity and rate performance. The researchers found that surface post-treatment or defect design can help deactivate surface oxygen, and induce the layered structure material to transform into a stable spinel structure. For example, $Li_{1.143}Mn_{0.544}Ni_{0.136}Co_{0.136}O_2$ is treated with a strong acid H_2SO_4 solution and then further annealed to prepare a defect-rich cathode material,[124] which effectively reduces the voltage drop while retaining a high specific discharge capacity (287 mAh g^{-1}). Surface modification of $Li_{1.144}Ni_{0.136}Co_{0.136}Mn_{0.544}O_2$ with CO_2 can create a large number of oxygen vacancies on the surface of the material.[125] Oxygen vacancies stabilize the lattice oxygen within the material structure and slow down the escape of oxygen, thereby improving ionic and electronic conductivity. Therefore, the material exhibits a high initial discharge specific capacity (301 mAh g^{-1}) without significant voltage drop.

The combination of bulk gradient design and single crystals is a strategy that eliminates the need of additional chemical elements and only changes the proportion of TMs in the synthesis process of Mn-based material precursors. The gradient configuration improves the electrochemical stability and thermal stability of Mn-LLO. In terms of single-crystal design, it offers multiple advantages, including excellent crystallinity, high mechanical/thermal stability, small surface area, and high tap density. Therefore, the degradation of single crystal materials, such as side reactions, cracking, and gas release, can be significantly inhibited.[77]

3.5 Critical comparison of optimization strategies

To provide a systematic understanding of the trade-offs among the core modification methods discussed above, a critical comparison of elemental doping, surface coating, and electrolyte additives, along with insights into their synergy, is presented/provided.

Elemental doping serves as a bulk-modification strategy that fundamentally regulates the crystal structure of Mn-based cathodes. Its primary advantage lies in addressing intrinsic structural defects, such as suppressing Jahn–Teller distortion of Mn^{3+} in spinel $LiMn_2O_4$, alleviating voltage decay of Li-rich layered oxides by stabilizing oxygen redox, and enhancing ionic conductivity through lattice engineering. However, this method typically requires precise control of doping elements, doping content, and high-temperature sintering processes, which increases the complexity of industrial production and may lead to uneven doping distribution if parameters are not optimized. It is particularly suitable for Mn-based materials suffering from bulk structural instability, such as layered $LiMnO_2$ and Li-rich oxides, where surface modification alone cannot resolve deep-seated phase transition issues.

Surface coating, as an interface-modification approach, forms a physical or chemical barrier between the cathode and electrolyte, which is highly effective in mitigating interfacial side reactions, inhibiting Mn dissolution, and preventing direct contact between active materials and electrolyte. Compared with elemental doping, it features relatively simple preparation processes (*e.g.*, sol–gel and wet chemical coating) and mild reaction conditions. Nevertheless, its limitations are evident: an excessively thick or poorly ionically conductive coating layer may introduce high interfacial impedance, reducing the rate performance of the cathode; moreover, the bonding force between the coating layer and the active material matrix may be insufficient, leading to coating peeling during long-term cycling. This strategy is preferred for high-voltage battery systems (*e.g.*, LIBs with operating voltage >4.5 V) and SIBs with aggressive electrolytes, where interfacial stability is the primary bottleneck.

Electrolyte additives offer a cost-effective and facile optimization route, as they can be directly incorporated into the electrolyte without modifying the cathode synthesis process. Their key advantage is the *in situ* formation of a high-quality CEI layer, which improves interfacial compatibility with minimal additional cost. However, their effect is largely limited to the electrode–electrolyte interface and cannot address bulk structural degradation, such as lattice distortion or irreversible phase transition. Additionally, the efficacy of additives is highly dependent on electrolyte composition and operating conditions, and excessive additive content may cause side reactions or reduce electrolyte ionic conductivity. This method is suitable as an auxiliary optimization strategy for cost-sensitive applications (*e.g.*, large-scale energy storage SIBs) or as a complement to bulk modification to further enhance interfacial stability.

In summary, these advanced strategies are essential for unlocking the full potential of Mn-based cathodes in next-generation energy storage systems. Element doping and surface coating, due to their simplicity and demonstrated effectiveness, remain the most widely explored methods, but their inherent limitations highlight the necessity of synergistic combinations (*e.g.*, bulk doping coupled with surface coating) to simultaneously address bulk structural instability and interfacial issues. Future research should focus on such integrated strategies, while also advancing the practicality of emerging methods like single-crystal synthesis, to further optimize the comprehensive performance of Mn-based cathodes.

4 Mechanism investigation

4.1 Characterization techniques

Despite significant advancements in Mn-based materials over the recent decades, their practical implementation in LIBs and SIBs remains hindered by persistent challenges, including the Jahn–Teller effect, Mn dissolution, oxygen release, and structural instability under ambient humidity. With the help of advanced characterization techniques, a comprehensive and in-

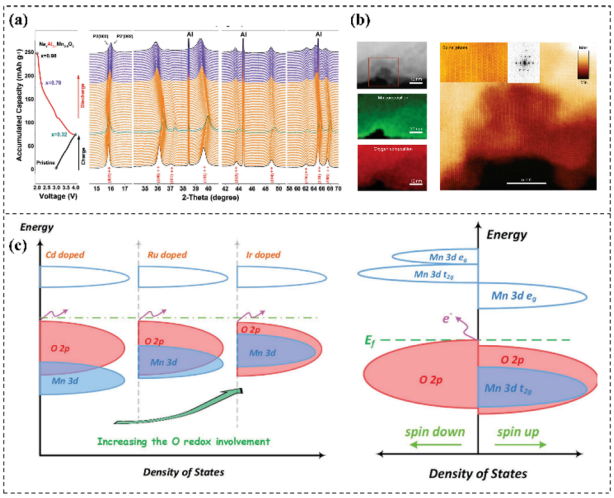

Fig. 6 (a) *In situ* synchrotron XRD during the initial charge–discharge cycle of Al-doped $Na_{0.67}MnO_2$. Reprinted with permission.[128] Copyright 2019 Wiley-VCH. (b) STEM-EELS mapping of the $Li_{1.2}Ni_{0.15}Co_{0.1}Mn_{0.55}O_2$ sample with an exposed pore. Reprinted with permission.[135] Copyright 2018 Springer Nature. (c) DOS for the selected potential doping species. Reprinted with permission.[142] Copyright 2019 Wiley-VCH.

depth understanding of the relationship between the electrochemical properties, structure, morphology, and composition of electrode materials can be established, enabling systematic evaluation ofthe effectiveness of modification strategies. In this section, we outline an overview of the advanced *ex situ* and *in situ*/*operando* characterization techniques used in the research of Mn-based materials during recent years.

Crystal structure analysis includes X-ray powder diffraction (XRD), neutron powder diffraction (NPD), and synchrotron X-ray diffraction (SXRD). XRD technology is based on a combination of Bragg reflection analysis and Rietveld refinement that can analyze the space groups, crystallinity, and oxygen vacancies of the material. NPD scattering technology has higher sensitivity to light elements (such as H, Li, and Na) that can effectively distinguish neighboring transition elements.[126] Therefore, NPD is often used as a supplement to XRD technology. SXRD based on high-energy X-rays demonstrates multiple advantages such as strong signal intensity, deep penetration, and short test time. Yabuuchi[127] synthesized the P2–$Na_{2/3}Fe_{1/2}Mn_{1/2}O_2$ and O3–$NaFe_{1/2}Mn_{1/2}O_2$ materials as cathodes for SIBs. SXRD was utilized to confirm the single phase of P2–$Na_{2/3}Fe_{1/2}Mn_{1/2}O_2$ and O3–$NaFe_{1/2}Mn_{1/2}O_2$. The two samples have different layered structures, with a hexagonal lattice with space group $P6_3/mmc$, and a rhombohedral lattice with space group $R3m$, respectively. Unlike XRD, pair distribution function (PDF) technology can directly obtain the interatomic distance inside the material, making it suitable for crystalline and amorphous materials. *In situ* or *operando* XRD characterization can be used to record the structural evolution to provide more reliable results. Liu[128] utilized the *in situ* synchrotron XRD characterization to track the P2 and P2′ phase transitions of Al-doped $Na_{0.67}MnO_2$ in the initial cycle, as shown in Fig. 6a. It was found that the Al-doped $Na_{0.67}MnO_2$ electrode exhibited a mild structural evolution compared with pristine $Na_{0.67}MnO_2$. The P2 phase remains unchanged throughout the charging process; during the discharge process, the (110) peak of the P2 phase disappears, and the (110) peak of the P2′ phase gradually appears.

X-ray PDF analysis compensates for the limited sensitivity of conventional XRD, enabling direct confirmation of TM migration from the TMO_2 layers to the interlayer space in Mn-rich Na_xTMO_2 materials under high-pressure conditions.[129] Beyond diffraction-based methods, when it comes to characterizing the microstructure and morphology, solid-state nuclear magnetic resonance (ss-NMR) spectroscopy offers distinct advantages as a non-destructive quantitative technique. Regarding microstructure and morphology-related techniques, ss-NMR spectroscopy is a non-destructive quantitative technique that is highly sensitive to the physical and chemical state of materials. It provides information such as the diffusion and migration of atoms or ions, offering mechanistic understanding of the relationship between the structural evolution and electrochemical performance of materials. ss-NMR enables investigation of the local distortion in the electronic structure and the P2–P2′ phase transitions in Mn-rich layered Na_xTMO_2 materials. Liu[128] conducted the ss-NMR characterization to study the local Na^+ environment of Al^{3+} doped P2–$Na_{0.67}MnO_2$ and pristine materials. Two unique signals are observed in the spectrum, where the sharp signal is located at 835 ppm and the broad signal is located at 1162 ppm, indicating that pristine materials are dominated by the P2′ phase. As the Al^{3+} doping content increases, the signal intensity of the P2′ phase decreases, which indicates that Al^{3+} doping favors the movement of Na^+ and reduces the Mn^{3+} Jahn–Teller center.

Raman spectroscopy is based on the inelastic scattering of photons caused by vibrations in the molecular structure.[130] Analyzing the peak shifts, intensities, and widths in a Raman spectrum can provide comprehensive insights into the local atomic environment and local structural ordering degree of materials. Due to the relatively weak signal, Raman spectroscopy is generally considered a bulk characterization technique. Compared with Raman spectroscopy, Fourier transform infrared (FTIR) spectroscopy has higher sensitivity and enhanced signal intensity, making it particularly effective for surface-sensitive analysis. This technique has proven highly valuable in assessing the humid air stability of Mn-based materials,[131,132] making great progress in monitoring electrolyte reduction, electrode degradation and formation of new species. *In situ* Raman spectroscopy has a high sensitivity to microstructural changes, enabling precise characterization of the oxygen-related redox process. Therefore, it can be well used to study phase transitions and the structural evolution during battery cycling, and widely applied in tracking the oxygen redox process in Mn-rich Na_xTMO_2 and Mn-LLO cathode materials. With the help of *in situ* Raman spectroscopy, the observation of real peroxo O–O bonds provides new evidence for reversible anionic redox chemistry in LRM cathode materials. For instance, Li[133] observed distinct variations in the peroxo O–O bond characteristics (length and vibrational position) between Li_2O_2 and H_2O_2 during charge/discharge cycling of

$Li_{1.2}Ni_{0.2}Mn_{0.6}O_2$. The observed peroxo O–O bond shortening during charging at the 4.5 V plateau quantitatively matches DFT predictions, validating the proposed coupling between Li/TM-layer delithiation/lithiation and peroxo bond formation/breaking as a unified redox mechanism. Differential electrochemical mass spectrometry (DEMS) can capture gas products during electrochemical cycling, making it possible to assist Raman spectroscopy technology to study reversible redox reactions, the formation of superoxide species, and the release of gaseous oxygen. The electrochemical behaviors and side reactions in moist air of Mn-based layered oxides in different electrolytes are revealed.[134]

SEM and TEM are the most traditional characterization techniques in the battery research area. With the upgrading of these two characterization techniques, especially the development of aberration correction technology, the resolution and detection sensitivity have improved. High-resolution transmission electron microscopy (HRTEM) and spherical aberration-corrected transmission electron microscopy are powerful technologies for obtaining high-resolution and even atomic-level structural information. In particular, when combined with selected area electron diffraction (SAED) and fast Fourier transform (FFT), more crystallographic information and structural evolution can be obtained. STEM combines the principles of SEM and TEM, becoming a mainstream technology for studying the structure, chemistry, and electronic state of electrode materials. HAADF and annular bright field (ABF) are two imaging modes used for capturing incoherent high-resolution Z-contrast images. EELS is a technique used to study the elemental composition, chemical bonds, oxidation state, and valence state of electrode materials. It can usually be coupled with STEM to obtain atomic-level structure and electronic information of electrode materials. In 2018, Hu[135] studied the $Li_{1.2}Ni_{0.15}Co_{0.1}Mn_{0.55}O_2$ electrode and found a large number of pores surrounded by Mn^{2+} thin shells. To further elucidate the source of these pores, STEM-EELS characterization was conducted, and it was found that with the exposition of the entire pore surface, a thick layer of a spinel/rock-salt structure phase was formed through the interaction between the pore surface and the electrolyte, as shown in Fig. 6b. Oxygen release in LMR materials reduces the average valence state of TM cations and causes microstructural defects, such as the formation of macropores within the particles, finally leading to voltage fade.

XPS is also a commonly used surface-sensitive technique. Since the binding energy of electrons depends on the atomic orbitals occupied by the electrons and the chemical environment of the atoms, XPS uses characteristic photoelectrons emitted by X-ray beams to analyze the elemental composition and oxidation states of the material surface. However, the probe depth of XPS is still limited to about 40 nm at 10.0 keV. XAS is one of the most popular spectroscopic techniques in materials research for chemical state and local structure analysis. The principle of XAS technology is the excitation of electrons to unoccupied states by absorbing the energy of incident X-ray photons; when the increased photon energy is sufficient to ionize the more tightly bound core electrons, the light absorption cross-section increases and can be observed, which is called the "absorption edge". Therefore, the characteristic energy levels of the electronic states of the respective elements can be determined by using the absorption edge. XAS mainly consists of three regions: pre-edge, XANES, and EXAFS. The energy range of about 50 eV before and after the absorption edge belongs to the XANES region, which is effective for probing the charge transfer and average oxidation state of 3d TMs. The energy range of about 50–1000 eV before and after the absorption edge belongs to the EXAFS region, which is effective for structural information, such as probing bond lengths and coordination numbers. XAS can also be divided into hard XAS (>5000 eV) and soft XAS (<3000 eV). Hard XAS can be used to study the charge compensation mechanism and the changes in the valence state. Soft XAS can be used to study anionic redox reactions. Keller utilized *in situ* XANES to study the redox processes of TMs in P2/P3/O3 type $Na_xMn_{0.5}Ni_{0.3}Fe_{0.1}Mg_{0.1}O_2$.[136] The spectra clearly show changes in the edge positions of Ni and Fe, while the Mn K edge position is essentially unaffected. The same general trend of energy increase for bulk Ni is also observed. The same energy increase at a relatively higher potential in Fe spectra is observed. Compared with the Mn K edge of O3-type materials, which shows a significant shift to higher energy, the Mn K edge of P2 and P2/P3/O3-type materials is not affected. Therefore, it is confirmed that P2-type and P2/P3/O3-type cathode materials have high cycle stability.

Resonant inelastic X-ray scattering (RIXS) is a bulk-sensitive technology with a large penetration depth that detects the localized electronic structure and the reversible oxygen redox of electrode materials. RIXS can absorb the primary photon and the secondary photon, probing changes in energy and momentum of scattered photons to provide more information about charge transfer and atomic species compared with XAS. Marie[137] employed high-resolution RIXS at the O K edge for quantitative analysis and tracked the changes in the formation of oxygen molecules during electrochemical cycling. Multiple RIXS scans were performed at different sample locations on $Li_{1.2}Ni_{0.13}Co_{0.13}Mn_{0.54}O_2$ in the charged state during the 2nd and 100th cycles. It was found that there were significant differences in oxygen activity during cycling. Throughout the charging process of the second cycle, a continuous increase in the amount of O_2 can be seen across the entire voltage range, which is reflected in the decrease in O_2 during the subsequent discharge process. It was confirmed that the loss of O-redox capacity and the voltage decay during cycling were caused by both the reduction in the reversibility of the O-redox process and the loss of oxygen. Therefore, they proposed that oxygen formed by the thermodynamic driving force leads to TM migration, void formation, and voltage decay in Mn-based Li-rich cathode materials. Mapping of RIXS (mRIXS) can further analyze the emission energy of emitted photons. According to the intensity change of the Mn L edge in mRIXS, the reversibility and cyclicity of the oxygen redox reaction can be quantified. To date, mRIXS has been widely used to detect the oxygen redox state of Mn-LLO[138] and Mn-rich Na_xTMO_2 materials.[139]

Other representative advanced characterization techniques, such as electron paramagnetic resonance (EPR)[140] and time-of-flight secondary-ion mass spectrometry (TOF-SIMS),[141] have also been developed to detect the oxidation state and electronic structure of bulk materials and quantitatively identify the composition and chemical state of element types on the surface, respectively.

4.2 Theoretical calculation/machine learning

With the accelerating global demand for energy storage, empirical studies alone have proven insufficient to direct the development of novel high-performance cathode materials for LIBs/SIBs. The powerful computing and theoretical calculations make it possible to predict and optimize the properties of Mn-based materials, such as indicating optimal ion diffusion paths, calculating migration energy barriers, and estimating electronic conductivity. DFT is a numerical technique based on first principles, calculations based on which have been reported since the late 1990s, and were subsequently applied to predict the structural parameters and electrochemical performance of rechargeable battery materials. DFT calculations can study the Li^+ migration path and activation energy barrier of spinel type $LiMn_2O_4$. Not only that, due to the Jahn–Teller effect, Mn dissolution and oxygen release problems in Mn-based materials, element doping, and coating are good improvement strategies. DFT can be used to study the surface and bulk Mn oxidation states and reaction properties. It has been confirmed that Mn^{4+} resides in the bulk phase, while the undesirable Mn^{3+} accumulates at the surface, attributed to its reduced coordination with O atoms. Additionally, studies show that metal oxides such as Al_2O_3 can modulate the valence state of O from +3 to +4. DFT calculations can also study the modification of Mn-based materials by surface doping. A series of transition metals (Ti, V, Cr, Fe, Co, Ni, Zr, and Nb) were screened as dopants, and calculations showed that Nb was optimal because its substitution enhances electronic conductivity, supplies extra electrons for charge compensation, and retards oxygen release during oxidation.[143] In addition, Nb atoms are more tightly bound to oxygen, which is beneficial for the electrochemically enhanced diffusion process in LIBs. For oxygen loss, DFT studies show that Co substitution leads to a reduction in the band gap of the cathode material, owing to the non-bonded metal energy band with a low energy value overlapping with the valence band, thus facilitating the loss of oxygen, while the Ti doping-induced band gap increase in the cathode material is attributed to the high energy of non-bonded metal bands.[144] Chen[145] used DFT calculations to study the Li extraction mechanism in Li_2MnO_3 and its correlation with oxygen release and structural transformation. It is shown that Li extraction is charge compensated by oxidation of the oxide anion and therefore the entire delithiation reaction involves lattice oxygen loss. Local holes on oxygen (O^-) are formed in the first step but are destabilized, leading to oxygen dimerization (O–O ~1.3 Å) and ultimately the formation of molecular O_2. Oxygen dimerization promotes Mn migration to octahedral sites in the vacated Li layer. The formation of the oxygen dimer O_2^{2-} then causes the migration of Mn ions, as the total energy becomes higher (structurally unstable) along the same migration path. Comparing the two reaction pathways, it appears that the oxygen dimer becomes more oxidized when coordinated with a smaller number of Mn cations. The configuration of the more oxidized oxygen dimer is thermodynamically more stable.

Regarding the utilization of DFT calculation in Mn-rich Na_xTMO_2 materials, DFT can be used to indicate the optimal ion diffusion paths, calculate migration energy barriers, and estimate the electronic conductivity. In particular, the projected density of states (PDOS) has been widely used to identify cation/anion band positions in Li/Na ion materials.[146] Zhang[142] conducted the DFT calculation to analyze the advantages and disadvantages of three doping metals, Cd, Ru, and Ir in the modification O3 type $Na_{1.2}Mn_{0.4}Ir_{0.4}O_2$ (DOS is shown in Fig. 6c). Since oxygen release is suppressed, the Cd, Ru, and Ir-doped Na–Mn–O system shows a trend of increasing O redox participation as the depth of Mn 3d band increases. Especially for Ir doping, the 3d energy band of Mn can be well embedded into the O 2p energy band with a higher energy level, forming a strong covalent Ir–O bond, effectively reducing the possibility of oxygen release. Li[56] used DFT calculations to simulate the air degradation mechanism of O3-type Na-rich layered materials. The bond dissociation energy (BDE) is an effective descriptor to predict the air stability of the O3 cathode. To understand the degradation mechanism of O3 layered oxides in ambient air, high-valent cations, such as Nb, Zr, and Ti were selected for doping and it was found that the reaction energy with ambient air became much more negative than that of $NaCoO_2$. Doping Mn (typically in the +4 oxidation state) renders the O3 material more degradation-prone, accounting for the air sensitivity of multiple Mn-based O3 cathodes. In contrast, doping Al, Cr, Li, Fe, Cu, Zn and Co themselves leads to higher reaction energies.

Theoretical calculation technology has great potential in predicting and evaluating Mn-based cathodes, and can further

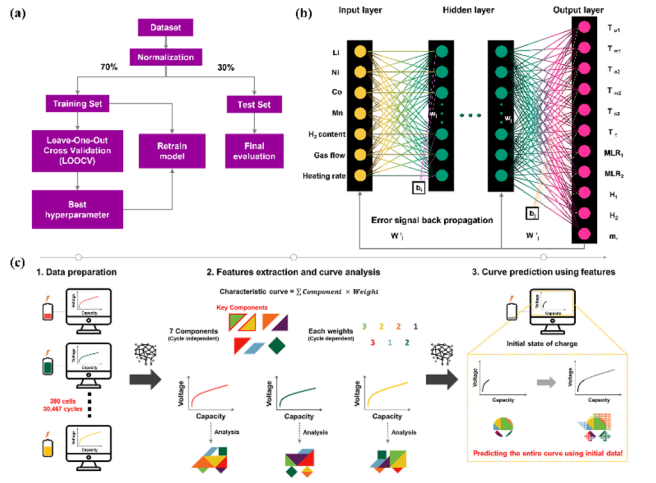

Fig. 7 (a) Training flow of the TG data prediction model and (b) architecture of the developed ANN model. Reprinted with permission.[150] Copyright 2025 OAE Publishing Inc. (c) Overview of PCA of charge curves of Li-rich layered cathode materials. Reprinted with permission.[151] Copyright 2025 Royal Society of Chemistry.

provide comprehensive guidance for Mn-based materials for LIB/SIB application. Nowadays, with the continuous deepening of scientific research exploration, machine learning (ML)-assisted screening and prediction of battery materials has been a powerful method for the reference values in material research.[147] From a microscopic perspective, ML can model the Hamiltonian of the system, enabling atomic-level property investigations. Concurrently, at macroscopic scales, ML can analyze macroscopic material characteristics such as hardness, melting point, and ductility. Comprehensive and accurate data collection, feature engineering, and model training and selection through cross-validation are crucial for establishing excellent ML models. ML also holds promise in analyzing phase structures and stability, and facilitating the design of functional materials.[148] Liu[149] reported that based on density functional theory calculations, machine learning and experimental validation, a multi-hierarchy screening of complex multi-element doping Li-rich layered cathode systems is developed using electrochemical activity, lattice strain, oxygen stability and transition metal migration barrier. It is further identified that the coupled polyhedral distortion parameter $D + \sigma^2$ of the substitution element is the most significant feature that affects the structural stability during cycling. The Li-rich layered cathode developed based on the predicted results exhibits remarkable long-term capacity stability (95.8% capacity retention over 300 cycles) and negligible voltage loss (0.02% voltage decay per cycle). The latest artificial neural network (ANN) machine learning methods perform well in handling nonlinear relationships and high-dimensional data. Huang[150] developed an ANN model to predict the key thermal decomposition parameters of Li-rich layered cathode materials and combined the analytic hierarchy process to quantify the thermal stability of cathode materials. This work proposes a method that can obtain key thermal decomposition information and quantitative risk assessment of cathode materials for LIBs without complex and repetitive thermogravimetric analysis tests (Fig. 7a and b). Park[151] proposed an unsupervised analysis framework that applies principal component analysis (PCA) to a large dataset of over 30 000 Li-rich layered cathode charge curves to analyze the attenuation mechanism of Li-rich cathodes, identify fundamental degradation factors and enhance predictability. By incorporating *ex situ* Mn L-edge and O K-edge soft XAS, along with electrochemical EIS, this work connects each principal component to physical phenomena such as Mn reduction and increasing charge-transfer resistance. Leveraging these insights, Park demonstrates robust predictive models that can accurately reconstruct full charge curves and reliably detect outliers or abnormal cycling patterns, as shown in Fig. 7c. Smarak Rath *et al.*[152] employed an eXtreme gradient boosting (XGBoost) classifier to classify direct-bandgap and indirect-bandgap materials, achieving an average accuracy of 72.8%. Houchins[153] utilized a density functional theory-based neural network model to predict the structural energy and force of various doped NCM materials, yielding promising accuracy. Wang *et al.*[154] applied gradient-boosting machine (GBM) models to observe the correlation between discharging performance and element/doping ratios in LIB cathodes, further predicting the chemical contents of NCM for high-performance cathode design. For Mn-based SIB cathode materials, Dong[155] compared GBM and random forest (RF) algorithms, demonstrating that GBM outperformed RF in predicting initial capacity (IC) and 50th cycle energy capacity (EC). Besides, cathode materials with a specific Na content ($0.75 < x < 1.25$), a dopant content ($x < 0.2$), and a nickel content ($x < 0.4$) seem to possess high values for both the IC and EC, which provide guidance for SIBs to design a new cathode. These results further encourage the application of ML methods to explore the complex structure–performance relationship of materials. Meanwhile, by bridging mechanistic domain knowledge learning with theoretical calculation technology, further underscoring the value of combining data-driven methodologies with mechanistic insights, this strategy can pave the way for more reliable and high-performance materials in next-generation battery systems.

Fig. 8 Comparison of commercialized NCM cathode materials and representative Mn-based materials.

5 Economic outlooks

When we develop cathode materials for rechargeable batteries, technical and economic aspects as well as potential environmental impacts should be considered (in Fig. 8). Herein, the life cycle assessment (LCA) and techno-economic analysis (TEA)[156] are utilized to evaluate commercialized $LiNi_xCo_yMn_zO_2$ (NCM) cathode materials and representative Mn-based materials, aiming to seek the possibility of Mn-based materials for future energy storage application. LCA is a system that is used to quantify inputs and outputs along product supply chains in terms of resources, carbon footprint, and environmental impacts.

The core materials in NCM and Mn-based cathodes are mainly Ni, Co, and Mn. In this section, we briefly review the different stages of production (including raw ore mining, smelting, and manufacturing), use, recycling, and disposal of these two types of cathodes, in order to compare the environmental and ecological impacts produced in these stages. The mainstream recycling routes for Mn-based cathode materials currently include pyrometallurgy, hydrometallurgy, and mechanochemistry. Pyrometallurgy is suitable for waste Mn-based batteries with high impurity content, achieving separation of Mn from other metals through high-temperature reduction; however, it is plagued by high energy consumption (approximately 8.5–10 kWh per kg) and potential Mn volatilization loss.[157] Hydrometallurgy, which adopts acid leaching-solvent extraction processes, has become the most widely

industrialized technology due to its high Mn recovery rate (92–96%) and relatively low energy consumption (3.2–4.5 kWh per kg).[158] Mechanochemistry, as an emerging green route, breaks the crystal structure *via* ball milling activation and enables gentle leaching conditions, reducing reagent consumption by over 30% while realizing synchronous recovery of Li, Mn, and other valuable elements.[157] In terms of industrial progress, hydrometallurgy has been scaled up in plants across China and Europe, with a processing capacity of 10 000–50 000 tons of waste Mn-based batteries per year.[158] Pyrometallurgy is mainly applied in scenarios with complex battery compositions, though its industrial promotion is restricted by high energy costs.[157] Mechanochemistry is currently in the pilot-scale stage, and several lab-scale technologies have demonstrated significant potential for industrialization following optimizations in equipment design and process parameters.[158]

For a more comprehensive LCA, a direct cost comparison between Mn-based materials and $LiFePO_4$ (LFP) in the recycling stage is further supplemented. The unit mass recycling cost of Mn-based cathode materials (dominated by hydrometallurgy) ranges from 1.5 to 2.2 $ per kg, slightly lower than that of $LiFePO_4$ (1.8 to 2.5 $ per kg).[157,159] This cost difference stems from two core aspects: first, Mn-based material recycling enables simultaneous recovery of high-value Mn and Li, while $LiFePO_4$ recycling mainly focuses on Li extraction with limited economic returns from Fe and P components; second, the acid leaching process of Mn-based materials requires lower reagent dosage due to the higher solubility of Mn oxides, reducing the cost of raw materials and wastewater treatment. From the perspective of full-life cycle cost accounting, the recycling stage accounts for 6–8% of the total full-life cycle cost of Mn-based battery systems, whereas this proportion reaches 8–10% for $LiFePO_4$ battery systems.[159] Additionally, the wastewater and residue treatment cost of Mn-based material recycling is approximately 0.3–0.5 $ per kg, lower than that of $LiFePO_4$ (0.4–0.6 $ per kg), attributed to the absence of complex Fe–P separation steps in Mn-based recycling processes.[158] This cost advantage further highlights the economic feasibility of Mn-based materials in large-scale energy storage applications.

Moreover, the correlation between costs (including production costs and transportation costs) and economic benefits would be comprehensively analyzed. Olivetti[160] found an increase in the ratio of known reserves to primary mine production (also known as the static loss index) for cobalt, Li, and natural graphite, suggesting that continued demand has led to additional exploration and mining. Mn and Ni showed no upward or downward trends, indicating that the ratio of production to known reserves remains relatively stable. Global Li raw materials mainly come from Australia, Chile, Argentina, and China. China is the largest producer and consumer of Li salts around the world. Stimulated by the high Li prices in the past two years, new and expanded Li projects around the world have gradually come into production, and supply and demand are balanced. There is consensus that supply risks for Co and Li are greater due to the concentration of known reserves and current production in the Democratic Republic of Congo (DRC). More than 60% of its current supply and half of its estimated reserves are located in the DRC, resulting in serious environmental and social impacts. The global supply of Ni raw materials mainly comes from the Republic of Indonesia. Driven by Chinese technology and capital, Indonesia has replaced China as the largest primary nickel producer in 2021, while China remains the world's largest Ni producer.

Based on the aforementioned raw material supply characteristics and cost differences, a quantitative comparison of core economic metrics and life-cycle carbon footprint between Mn-based cathodes and mainstream commercial materials (NCM811 and LFP) is supplemented herein, drawing from peer-reviewed LCA studies and industry production data,[161,162] to further clarify their commercial competitiveness. In terms of raw material cost per kg, Mn-based cathodes (*e.g.*, Li-rich Mn-based oxides and tunnel-type Na_xMnO_2) range from 15–25 $ per kg, significantly lower than NCM811 (45–60 $ per kg) which relies on high-cost Ni and Co, and moderately competitive with LFP (20–30 $ per kg). This advantage originates from the abundant and low-cost manganese ore (~1.5 $ per kg), in contrast to Ni ore (~15 $ per kg) and Co ore (~80 $ per kg) for NCM811. From the perspective of total cradle-to-gate production cost, Mn-based cathodes are estimated at 30–40 $ per kg, compared to 60–80 $ per kg for NCM811 and 35–45 $ per kg for LFP, reinforcing their cost potential in large-scale energy storage. In terms of the life-cycle carbon footprint, the cradle-to-gate carbon footprint of Mn-based cathodes is 12–18 kg CO_2-eq per kg, 30–40% lower than that of NCM811 (20–28 kg CO_2-eq per kg) due to the avoidance of energy-intensive Ni/Co mining and refining. Compared with LFP (10–16 kg CO_2-eq per kg), Mn-based cathodes have a comparable carbon footprint profile, with the minor gap attributed to additional energy for structural modification. A stage-wise breakdown shows that raw material extraction contributes only 2–3 kg CO_2-eq per kg for Mn-based cathodes, far lower than 8–12 kg for NCM811, while the manufacturing stage (40–50% of the total carbon footprint) and end-of-life disposal (<10%) are consistent with or lower than those of their commercial counterparts.

In the manufacturing energy consumption aspect, different statistical approaches also confirm the environmental advantage of Mn-based cathodes. Dunn[163] reported that the manufacturing energy consumption of NCM cathode materials is two to three times higher than that of Mn-based materials, such as $LiMn_2O_4$ (LMO). For NCM cathode materials, production usually includes two main stages: co-precipitation and calcination. Metal nitrate, metal sulfate, or metal acetate and hydroxide react in a continuous mixing kettle reactor to form $Ni_xMn_yCo_z(OH)_2$, and then separate and recycle solvents to dry. Because the total precipitation will produce wastewater containing ammonia and sodium sulfate, it also needs to be treated for appropriate disposal or reuse, which may lead to the nutritionalization of water. Most of the energy demand related to co-precipitation can be attributed to wastewater treatment, and the rest is attributed to direct production and environmental control and dryness of $Ni_xMn_yCo_z(OH)_2$ in the reactor. A total of 11.8 kWh calories is consumed to produce 1 kg $Ni_xMn_yCo_z(OH)_2$, but the energy consumed will vary under specific conditions. The calcination stage needs to use high-temperature

sintering materials for $Ni_xMn_yCo_z(OH)_2$ and Li compounds (usually hydroxide or carbonate) to eventually produce NCM active materials. In addition, more processes of calcination may be required, because the primary task of manufacturers is to maximize production rather than reduce energy consumption. It is known that the combustion process for producing 1 kg of NCM active material comsumes 7.0 MJ of electricity. However, the type of fuel and energy concumption may vary depending on specific circumstances. LMO cathode materials can be produced through various methods, including solid-state, solution-gel, hydrothermal, and combustion procedures. The energy intensity of LMO production is 5.0 kWh per kg compared with that of NCM.

TEA is designed to evaluate the performance parameters and economic feasibility of a product. Yi[10] proposed that the price per kWh of Mn-based materials is lower than that of present NCM materials by calculating the preparation cost, including that of raw materials and preparation technology. For electric vehicles, gravimetric energy density (GED) and material cost are more important than volumetric energy density (VED) because it has more space and uses more batteries to produce more energy. Although NCM materials, such as NCM523 and NCM811, have much lower VED than $LiCoO_2$, their GED is comparable to that of $LiCoO_2$. NCM is widely used in electric vehicle batteries due to its significantly cheaper material cost compared to $LiCoO_2$. Although $LiFePO_4$ has a relatively lower GED than NCM and $LiCoO_2$, it remains a viable cathode material for electric vehicles due to its lower cost per kWh and extremely long life. The cost per kWh of $LiFePO_4$ is 20.9 $ per kWh. Mn-based materials with cost less than NCM (NCM523: 47.5 $ per kWh; NCM811: 47.5 $ per kWh) can be considered as potential cathode materials.

Among these low-priced manganese-based materials, spinel LMO and $LiNi_{0.5}Mn_{1.5}O_4$ have the lowest cost per watt hour, at 18.1 $ per kWh. LMO has been applied to two-wheel electric vehicles and power tools that require high-cost performance and can withstand relatively low energy density and cycle performance. The GED of layered $LiNi_{0.5}Mn_{0.5}O_2$ is comparable to that of NCM523, and its kWh cost (26.5 $ per kWh) is much lower than that of NCM523. It has the potential to replace NCM materials because of its low price. The cost for LRM materials such as layered $Li_{1.2}Ni_{0.2}Mn_{0.6}O_2$ (26.5 $ per kWh, 0.825 kWh kg^{-1}) and rock salt $Li_{1.2}Mn_{0.625}Nb_{0.175}O_{1.95}F_{0.05}$ (41.9 $ per kWh, 1.056 kWh kg^{-1}) are reduced. The cost per Wh of $LiMnPO_4$ (22.3 $ per kWh) and $LiMn_{0.5}Fe_{0.5}PO_4$ (20.9 $ per kWh) is similar to that of $LiFePO_4$, showing considerable advantages in price.

6 Summary and outlook

Manganese (Mn)-based cathode materials are promising candidates for next-generation rechargeable batteries (LIBs/SIBs) due to their low cost, low toxicity, high natural abundance, variable valence state-enabled diverse crystal structures, and high energy density, making them particularly attractive for sustainable energy storage applications. However, their further development and commercialization are hindered by inherent challenges, and in this review, the composition, performance limitations, optimization strategies, research techniques, and future directions of Mn-based cathodes are systematically analyzed and summarized.

(1) Current Mn-based cathode materials suffer from inherent issues including Jahn–Teller deformation, Mn dissolution, oxygen release, and poor air instability. These problems lead to progressive crystal structure degradation during prolonged cycling, thereby causing the deterioration of electrochemical performance. To address these challenges, multiple optimization strategies such as surface modification and coating have been developed, which effectively enhance the structural stability and kinetic properties of Mn-based cathodes, resulting in significant improvements in both cycling stability and rate capability. Future research needs to further optimize these strategies, especially developing efficient, cost-effective, and scalable surface engineering methods to lay a foundation for commercialization.

(2) Combining multiple physical characterization techniques is of great significance for understanding and developing Mn-based cathode materials. This review summarizes advanced *in situ*/*operando* characterization methods, which are applied to study the surface properties of Mn-based cathodes (including the crystal structure, electronic structure, oxidation state of transition metal (TM) ions, and doping effect) as well as the mechanisms of Mn dissolution and oxygen release. Besides, the important role of density functional theory (DFT) research in screening and predicting the structural properties of Mn-based cathodes is also reviewed. To deeply elucidate the reaction mechanism of Mn-based cathodes, future studies should adopt advanced high-energy, high-resolution characterization strategies combined with high-throughput computing and machine learning, providing insights for designing Mn-based cathodes with optimal performance.

(3) From the perspective of industrial application and market development, most current research on Mn-based cathodes remains at the laboratory scale, and the lack of scalable preparation technologies and systematic commercial feasibility evaluation restricts their transition to industrial production. Techno-economic analysis and life-cycle assessment of Mn-based cathodes in sustainable energy storage need to be further supplemented to comprehensively evaluate their commercial potential.

While the aforementioned strategies address key bottlenecks of Mn-based cathodes in conventional liquid electrolyte systems, exploring their compatibility with solid-state electrolytes opens up a pivotal new frontier that is essential for advancing their application in next-generation high-safety, high-energy-density batteries.

Current studies indicate that such compatibility varies significantly with the type of solid-state electrolytes: for sulfide electrolytes (*e.g.*, Li_3PS_4 and $Li_{10}GeP_2S_{12}$), the dissolution and migration of Mn^{2+} tend to trigger interfacial side reactions (*e.g.*, formation of MnS impurity phases), resulting in elevated interfacial impedance. This issue can be effectively mitigated by surface coating of Mn-based materials (*e.g.*, Al_2O_3 and Li_3PO_4) or heteroatom doping of electrolytes, which effectively suppresses interfacial side reactions and improves cycling

stability.[164] For oxide electrolytes (*e.g.*, $Li_7La_3Zr_2O_{12}$ and $Li_{1.3}Al_{0.3}Ti_{1.7}(PO_4)_3$), the air instability of Mn-based materials may exacerbate the formation of oxygen vacancies at the interface, impeding ion conduction efficiency. Optimizing sintering processes (*e.g.*, low-temperature co-sintering) and regulating surface chemical states can improve interfacial contact and charge transfer kinetics, thereby reducing interfacial resistance.[165] Notably, Mn-based materials with unique crystal structures (*e.g.*, tunnel-type $Na_{0.44}MnO_2$ and olivine-type $LiMnPO_4$) exhibit inherent compatibility advantages with solid-state electrolytes, attributed to their stable frameworks and low Mn dissolution tendency.

Beyond LIBs and SIBs, Mn-based cathodes also demonstrate considerable potential in various emerging battery systems, including potassium-ion batteries (PIBs), aqueous rechargeable batteries (ARBs), and all-solid-state batteries (ASSBs). Their unique advantages and inherent challenges in each system are analysed as follows to broaden the scope of the application prospect discussion:

For potassium-ion batteries (PIBs), Mn-based materials such as tunnel-type K_xMnO_2 and layered KMn_2O_4 stand out due to their low cost, high theoretical capacity, and favorable structural adaptability to the large ionic radius of K^+. Their open crystal frameworks can accommodate K^+ intercalation/deintercalation with relatively small volume expansion, which is a critical advantage over many other cathode candidates for PIBs. Nevertheless, they face prominent challenges: severe K^+ diffusion impedance caused by the large ionic size, structural degradation from repeated intercalation–extraction cycles of K^+, and low initial coulombic efficiency induced by electrolyte decomposition on the cathode surface. Surface modification strategies like carbon coating and heteroatom doping (*e.g.*, Al and Fe doping) have been proven effective in mitigating these issues by enhancing electron conductivity, stabilizing the crystal structure, and suppressing side reactions.

In aqueous rechargeable batteries (ARBs), Mn-based cathodes (*e.g.*, MnO_2 polymorphs and Mn_3O_4) are highly competitive due to their low toxicity, environmental benignity, and excellent redox activity in aqueous electrolytes. They can be paired with low-cost anodes such as Zn, Fe, and Al to construct high-safety, low-cost aqueous battery systems, which are promising for large-scale energy storage and wearable electronics. The main challenges restricting their practical application include Mn dissolution in aqueous electrolytes (especially under acidic or alkaline conditions), poor cycling stability arising from irreversible phase transitions, and a narrow voltage window limited by water splitting. Optimizing electrolyte compositions (*e.g.*, adding Mn^{2+} additives to suppress dissolution and using gel electrolytes to widen the voltage window) and constructing protective interfaces (*e.g.*, metal oxide coating) are promising approaches to improve their cycling stability and electrochemical performance.

For all-solid-state batteries (ASSBs), building on the aforementioned compatibility discussion, Mn-based cathodes exhibit unique advantages such as high redox potential, good compatibility with partial solid electrolytes (*e.g.*, tunnel-type Mn-based materials with sulfide electrolytes), and cost competitiveness compared to Ni/Co-based cathodes. These merits make them potential candidates for low-cost ASSBs. The core challenges remain interfacial issues: interfacial side reactions between Mn-based cathodes and solid electrolytes, poor interfacial contact due to rigid solid–solid interaction, and performance degradation induced by Mn dissolution. As discussed earlier, surface coating, electrolyte modification, and optimized sintering processes are effective strategies to alleviate these interfacial problems, laying the groundwork for their application in ASSBs.

Future research should focus on the precise regulation of interfacial reaction mechanisms, the development of low-cost compatible solid-state electrolytes, and the integration optimization of all-solid-state battery devices, which will lay a solid foundation for the large-scale application of Mn-based materials in next-generation energy storage systems. Overall, Mn-based cathode materials have great potential in next-generation high-performance LIBs and SIBs; intensifying efforts to solve existing problems (such as structural instability, limited characterization depth, and immature commercialization technologies) will accelerate the explosive growth of the rechargeable battery market.

Author contributions

H. Z., T. Y., and X. W. wrote and edited the original draft. All authors contributed to the figures, review, and editing of the manuscript.

Conflicts of interest

There are no conflicts to declare.

Data availability

The data that support the findings of this study are available from the corresponding author upon reasonable request.

Acknowledgements

The work was supported by the National Natural Science Foundation of China (52502270). The authors also acknowledge the support from the Ministry of Human Resources and Social Security's Funding Scheme for High-Level Overseas Chinese Talents' Return, and the Program for Jiangsu Specially-Appointed Professors.

References

1 B. Dunn, H. Kamath and J. M. Tarascon, Electrical energy storage for the grid: A battery of choices, *Science*, 2011, **334**, 928–935.
2 J. M. Tarascon and M. Armand, Issues and challenges facing rechargeable lithium batteries, *Nature*, 2001, **414**, 359–367.
3 T. T. Zeng, D. H. Liu, C. L. Fan, R. Z. Fan, F. Q. Zhang, J. S. Liu, T. Z. Yang and Z. W. Chen, $LiMn_{0.8}Fe_{0.2}PO_4$@C

cathode prepared via a novel hydrated $MnHPO_4$ intermediate for high performance lithium-ion batteries, *Inorg. Chem. Front.*, 2023, **10**, 1164–1175.

4 N. Yabuuchi, K. Kubota, M. Dahbi and S. Komaba, Research development on sodium-ion batteries, *Chem. Rev.*, 2014, **114**, 11636–11682.

5 C. P. Grey and J. M. Tarascon, Sustainability and in situ monitoring in battery development, *Nat. Mater.*, 2016, **16**, 45–56.

6 J. Song, H. C. Wang, Y. X. Zuo, K. Zhang, T. H. Yang, Y. L. Yang, C. Gao, T. Chen, G. Feng, Z. W. Jiang, W. K. Xiao, T. Luo and D. G. Xia, Building better full manganese-based cathode materials for next-generation lithium-ion batteries, *Electrochem. Energy Rev.*, 2023, **6**, 20–57.

7 H. X. Li, W. Zhang, K. N. Sun, J. Guo, K. Yuan, J. J. Fu, T. Zhang, X. K. Zhang, H. W. Long, Z. A. Zhang, Y. Q. Lai and H. Y. Sun, Manganese-based materials for rechargeable batteries beyond lithium-ion, *Adv. Energy Mater.*, 2021, **11**, 2100867–2100901.

8 W. He, W. B. Guo, H. L. Wu, L. Lin, Q. Liu, X. Han, Q. S. Xie, P. F. Liu, H. F. Zheng, L. S. Wang, X. Q. Yu and D. L. Peng, Challenges and recent advances in high capacity Li-rich cathode materials for high energy density lithium-ion batteries, *Adv. Mater.*, 2021, **33**, 2005937–2005972.

9 Z. Y. Gu, X. T. Wang, Y. L. Heng, Y. Liu, S. H. Zheng, K. Y. Zhang, Z. L. Hao and X. L. Wu, Polyanionic cathodes for sodium-ion batteries: Materials, working mechanism, and applications, *Mater. Sci. Eng. R Rep.*, 2025, **165**, 101008–101045.

10 H. M. Yi, Y. Liang, Y. L. Qian, Y. C. Feng, Z. Li and X. Zhang, Low-cost Mn-based cathode materials for lithium-ion batteries, *Batteries*, 2023, **9**, 246–268.

11 X. B. Lou, Z. L. Li, S. N. Kang, Y. F. Li, S. Ma, F. S. Geng and B. W. Hu, In situ electron paramagnetic resonance reveals fading mechanism of Mn-based prussian blue analogue: Accelerated Mn dissolution due to charge delocalization, *Renewables*, 2024, **2**, 341–352.

12 M. M. Thackeray and K. Amine, $LiMn_2O_4$ spinel and substituted cathodes, *Nat. Energy*, 2021, **6**, 566.

13 G. Sun, Z. Y. Song, Y. M. Dai, Q. Yu, Q. Kang, Z. Q. Wang, Y. W. Chen, Y. P. Shi, S. X. Qiao, Z. K. Xiao and W. Luo, Molten salt synthesis of a single-crystal $LiNi_{0.5}Mn_{1.5}O_4$ cathode with an in situ constructed stable interface for 4.8 V-class all-solid-state batteries, *Sci. China Mater.*, 2025, **68**, 2006–2013.

14 S. Maiti, H. Sclar, R. Konar, J. Grinblat, M. Talianker, K. Keinan-Adamsky, B. Markovsky, X. H. Wu, A. Kondrakov and D. Aurbach, Improving the performance of $LiNi_{0.5}Mn_{1.5}O_4$ cathode based high-voltage lithium-ion batteries via manipulating the electrolyte solution with trimesic and terephthalic acids, *Mater. Today*, 2025, **89**, 1–11.

15 J. W. Lim, J. H. Kim, D. H. Park, J. S. Jang, W. C. Kim, S. Y. Ahn, G. I. Lee, J. M. Hong, S. J. Park, M. J. Kim, S. Y. Jang and K. W. Park, Enhanced electrochemical stability of solid-state electrolyte-coated high-voltage $LiNi_{0.5}Mn_{1.5}O_4$ cathodes in Li-ion batteries, *Energy Environ. Mater.*, 2025, **8**, e70025.

16 K. Tokiwa, K. Matsukura, S. Kasahara, S. Tsuda, S. Mikusu, K. Takeuchi, A. Iyo, Y. Tanaka, J. Akimoto, J. Awaka, N. Kijima, Y. Takahashi and T. Watanabe, High pressure synthesis and magnetic properties of $CaFe_2O_4$-type $NaMn_2O_4$ and $LiMn_2O_4$, *J. Phys. Conf. Ser.*, 2009, **150**, 042210–042213.

17 X. Z. Liu, X. Wang, A. Iyo, H. J. Yu, D. Li and H. S. Zhou, High stable post-spinel $NaMn_2O_4$ cathode of sodium ion battery, *J. Mater. Chem. A*, 2014, **2**, 14822–14826.

18 M. K. Datta, R. Kuruba, P. H. Jampani, S. J. Chung, P. Saha, R. Epur, K. Kadakia, P. Patel, B. Gattu, A. Manivannan and P. N. Kumta, Electrochemical properties of a new nanocrystalline $NaMn_2O_4$ cathode for rechargeable sodium ion batteries, *Mater. Sci. Eng., B*, 2014, **188**, 1–7.

19 C. Ling and F. Mizuno, Phase stability of post-spinel compound AMn_2O_4 (A = Li, Na, or Mg) and its application as a rechargeable battery cathode, *Chem. Mater.*, 2013, **25**, 3062–3071.

20 Q. D. Wang, Z. P. Yao, J. L. Wang, H. Guo, C. Li, D. Zhou, X. D. Bai, H. Li, B. H. Li, M. Wagemaker and C. L. Zhao, Chemical short-range disorder in lithium oxide cathodes, *Nature*, 2024, **629**, 341–347.

21 S. X. Zhao, H. X. Liu, S. X. Ouyang and Q. Li, Synthesis and performance of $LiMnO_2$ as cathodes for Li-ion batteries, *J. Wuhan Univ. Technol. Mater. Sci. Ed.*, 2003, **18**, 5–8.

22 M. Rossouw and M. Thackeray, Lithium manganese oxides from Li_2MnO_3 for rechargeable lithium battery applications, *Mater. Res. Bull.*, 1991, **26**, 463–473.

23 P. Kalyani, S. Chitra, T. Mohan and S. Gopukumar, Lithium metal rechargeable cells using Li_2MnO_3 as the positive electrode, *J. Power Sources*, 1999, **80**, 103–106.

24 J. X. Guo, Z. C. Jian, Y. F. Zhu, Q. C. Ling, M. Y. Li, X. Y. Liu, H. S. Xin and Y. Xiao, Low-cost Mn-based P2/O3 heterostructured layered oxide cathodes based on orbital-lattice synergistic modulation strategy for sodium-ion batteries, *Sci. China Mater.*, 2025, **68**, 3685–3694.

25 Z. X. Huang, K. Li, J. M. Cao, K. Y. Zhang, H. H. Liu, J. Z. Guo, Y. Liu, T. Wang, D. M. Dai, X. Y. Zhang, H. B. Geng and X. L. Wu, New insights into anionic redox in P2-type oxide cathodes for sodium-ion batteries, *Nano Lett.*, 2024, **24**, 13615–13623.

26 X. Y. Cai, Z. Shadike, N. Wang, X. L. Li, Y. Wang, Q. F. Zheng, Y. X. Zhang, W. X. Lin, L. S. Li, L. W. Chen, S. Y. Shen, E. Y. Hu, Y. N. Zhou and J. L. Zhang, Constraining interlayer slipping in P2-type layered oxides with oxygen redox by constructing strong covalent bonds, *J. Am. Chem. Soc.*, 2025, **147**, 5860–5870.

27 Q. Ding, W. H. Zheng, A. Zhao, Y. N. Zhao, K. Chen, X. Zhou, H. Y. Zhang, Q. Y. Li, X. P. Ai, H. X. Yang, Y. J. Fang and Y. L. Cao, W-doping induced efficient tunnel-to-layered structure transformation of $Na_{0.44}Mn_{1-x}W_xO_2$: Phase evolution, sodium-storage properties, and moisture stability, *Adv. Energy Mater.*, 2023, **13**, 2203802–2203812.

28 T. W. Cui, X. Li, Y. B. Si and Y. Z. Fu, Synergetic anion-cation co-doping in $Na_{0.44}MnO_2$ boosting a high-stability and

improved-kinetics cathode for sodium ion battery, *Energy Storage Mater.*, 2024, **65**, 103161–103168.

29 Y. Xiao, Q. Q. Sun, D. C. Chen, J. Q. Wang, J. J. Ding, P. Tan, Y. Sun, S. L. Zhang, P. F. Wang, J. F. Mao and Y. F. Zhu, Guideline of dynamic tunnel structural evolution for durable sodium-ion oxide cathodes, *Adv. Mater.*, 2025, **37**, 2504312–2504324.

30 Y. S. Wang, J. Liu, B. Lee, R. M. Qiao, Z. Z. Yang, S. Y. Xu, X. Q. Yu, L. Gu, Y. S. Hu, W. L. Yang, K. Kang, H. Li, X. Q. Yang, L. Q. Chen and X. J. Huang, Ti-substituted tunnel-type $Na_{0.44}MnO_2$ oxide as a negative electrode for aqueous sodium-ion batteries, *Nat. Commun.*, 2015, **6**, 6401–6410.

31 T. E. Fan, S. M. Liu, X. Tang, Z. H. Zou, J. Q. Xie and M. Y. Wang, Rational construction of $Na_{0.44}MnO_2$ nanorods and PAN nanofibers composite as high areal capacity sodium-ion batteries, *Ionics*, 2021, **27**, 1137–1142.

32 H. Y. Zhang, Y. H. Xiang, B. C. Liu, G. Li, C. Dun, H. Y. Huang, Q. L. Zou, L. Z. Xiong and X. W. Wu, Fe doping mechanism of $Na_{0.44}MnO_2$ tunnel phase cathode electrode in sodium-ion batteries, *J. Colloid Interface Sci.*, 2024, **661**, 389–400.

33 A. K. Padhi, K. S. Nanjundaswamy and J. B. Goodenough, Phospho-olivines as positive-electrode materials for rechargeable lithium batteries, *J. Electrochem. Soc.*, 1997, **144**, 1188–1194.

34 H. Zhang, Z. Y. Gu, X. T. Wang, X. X. Zhao, Y. L. Heng, Y. Liu, J. L. Yang, S. H. Zheng and X. L. Wu, Electronic confinement-restrained Mn_{Na} anti-site defects in sodium-rich phosphates toward multi-electron transfer and high energy efficiency, *Adv. Mater.*, 2024, **36**, 2410797–2410806.

35 T. Boyadzhiev, V. Koleva, E. Zhecheva, D. Nihtianova, L. Mihaylov and R. Stoyanova, Competitive lithium and sodium intercalation into sodium manganese phospho-olivine $NaMnPO_4$ covered with carbon black, *RSC Adv.*, 2015, **5**, 87694–87705.

36 M. Y. Pan, S. T. Lu, M. Y. Zhang, C. Li, G. D. Zou, K. Z. Cao and Y. Fan, Synthesis of olivine $NaMnPO_4$ single crystals and electrochemical performance as anode material for Li-ion batteries, *J. Solid State Chem.*, 2023, **321**, 123929–123934.

37 L. Yang, W. T. Deng, W. Xu, Y. Tian, A. N. Wang, B. W. Wang, G. Q. Zou, H. S. Hou, W. N. Deng and X. B. Ji, Olivine $LiMn_xFe_{1-x}PO_4$ cathode materials for lithium ion batteries: Restricted factors of rate performances, *J. Mater. Chem. A*, 2021, **9**, 14214–14232.

38 T. A. Wani and G. Suresh, A comprehensive review of $LiMnPO_4$ based cathode materials for lithium-ion batteries: Current strategies to improve its performance, *J. Energy Storage*, 2021, **44**, 103307–103363.

39 T. Boyadzhieva, V. Koleva, R. Kukeva, D. Nihtianova, S. Harizanova and R. Stoyanova, Storage performance of Mg^{2+} substituted $NaMnPO_4$ with an olivine structure, *RSC Adv.*, 2020, **10**, 29051–29060.

40 V. Priyanka, G. Savithiri, P. Rajkumar, T. Meenatchi, R. Subadevi and M. Sivakumar, Tweaking the electrochemical activity of maricite $NaMnPO_4$ in sodium batteries using different manganese precursors via polyol method, *J. Solid State Chem.*, 2020, **290**, 121551–121557.

41 A. K. Padhi, K. S. Nanjundaswamy and J. B. Goodenough, Phospho-olivines as positive-electrode materials for rechargeable lithium batteries, *J. Electrochem. Soc.*, 1997, **144**, 1188–1194.

42 A. Yamada, S. C. Chung and K. Hinokuma, Optimized $LiFePO_4$ for lithium battery cathodes, *J. Electrochem. Soc.*, 2001, **148**, A224–A229.

43 C. Delacourt, L. Laffont, R. Bouchet, C. Wurm, J. B. Leriche, M. Morcrette, J. M. Tarascon and C. Masquelier, Toward understanding of electrical limitations (electronic, ionic) in $LiMPO_4$ (M = Fe , Mn) electrode materials, *J. Electrochem. Soc.*, 2005, **152**, A913–A921.

44 I. M. Nwachukwu, A. C. Nwanya, A. B. C. Ekwealor and F. I. Ezema, Research progress in solid-state synthesized $LiMnPO_4$ cathode material for Li-ion battery applications, *Appl. Surf. Sci. Adv.*, 2023, **18**, 100505–100521.

45 L. Y. Liu, G. Y. Chen, B. T. Du, Y. Y. Cui, X. Ke, J. Liu, Z. P. Guo, Z. C. Shi, H. Y. Zhang and S. L. Chou, Nano-sized cathode material $LiMn_{0.5}Fe_{0.5}PO_4$/C synthesized via improved sol-gel routine and its magnetic and electrochemical properties, *Electrochim. Acta*, 2017, **255**, 205–211.

46 T. Luo, T. T. Zeng, S. L. Chen, R. Li, R. Z. Fan, H. Chen, S. C. Han and C. L. Fan, Structure, performance, morphology and component transformation mechanism of $LiMn_{0.8}Fe_{0.2}PO_4$/C nanocrystal with excellent stability, *J. Alloys Compd.*, 2020, **834**, 155143–155156.

47 S. Narukawa, Y. Takeda, M. Nishijima, N. Imanishi, O. Yamamoto and M. Tabuchi, Anti-fluorite type Li_6CoO_4 , Li_5FeO_4, and Li_6MnO_4 as the cathode for lithium secondary batteries, *Solid State Ionics*, 1999, **122**, 59–64.

48 J. Lee, A. Urban, X. Li, D. Su, G. Hautier and G. Ceder, Unlocking the potential of cation-disordered oxides for rechargeable lithium batteries, *Science*, 2014, **343**, 519–522.

49 J. Lee, D. A. Kitchaev, D. H. Kwon, C. W. Lee, J. K. Papp, Y. S. Liu, Y. L. Zheng, R. J. Clément, T. Shi, B. D. Mccloskey, J. H. Guo, M. Balasubramanian and G. Ceder, Reversible Mn^{2+}/Mn^{4+} double redox in lithium-excess cathode materials, *Nature*, 2018, **556**, 185–190.

50 H. T. Liu, Y. M. Zhao, H. Zhang, X. Lian, Y. Z. Dong and Q. Kuang, Structural and electrochemical properties of Fe-doped $Na_2Mn_{3-x}Fe_x(P_2O_7)_2$ cathode material for sodium ion batteries, *J. Power Sources*, 2017, **370**, 114–121.

51 C. L. Xu, R. J. Xiao, J. M. Zhao, F. X. Ding, Y. Yang, X. H. Rong, X. D. Guo, C. Yang, H. Z. Liu, B. H. Zhong and Y. S. Hu, Mn-rich phosphate cathodes for Na-ion batteries with superior rate performance, *ACS Energy Lett.*, 2021, **7**, 97–107.

52 H. A. Jahn and E. Teller, Stability of polyatomic molecules in degenerate electronic states, *Proc. R. Soc. Lond.*, 1937, **161**, 220–235.

53 T. C. Liu, A. Dai, J. Lu, Y. F. Yuan, Y. G. Xiao, L. Yu, M. Li, J. Gim, L. Ma, J. J. Liu, C. Zhan, L. X. Li, J. X. Zheng, Y. Ren, T. P. Wu, R. Shahbazian-Yassar, J. G. Wen, F. Pan and K. Amine, Correlation between manganese

dissolution and dynamic phase stability in spinel-based lithium-ion battery, *Nat. Commun.*, 2019, **10**, 4721–4731.

54 B. Cao, T. Y. Li, W. G. Zhao, L. Yin, H. B. Cao, D. Chen, L. X. Li, F. Pan and M. J. Zhang, Correlating rate-dependent transition metal dissolution between structure degradation in Li-rich layered oxides, *Small*, 2023, **19**, 2301834–2301842.

55 S. P. Jia, S. Kumakura and E. McCalla, Unravelling air/moisture stability of cathode materials in sodium ion batteries: Characterization, rational design, and perspectives, *Energy Environ. Sci.*, 2024, **17**, 4343–4389.

56 H. L. Li, J. Y. Wang, S. Xu, A. Y. Chen, H. Y. Lu, Y. Jin, S. H. Guo and J. Zhu, Universal design strategy for air-stable layered Na-ion cathodes toward sustainable energy storage, *Adv. Mater.*, 2024, **36**, 2403073–2403084.

57 Q. Li, G. S. Li, C. C. Fu, D. Luo, J. M. Fan and L. P. Li, K^+ doped $Li_{1.2}Mn_{0.54}Co_{0.13}Ni_{0.13}O_2$: A novel cathode material with an enhanced cycling stability for lithium-ion batteries, *ACS Appl. Mater. Interfaces*, 2014, **6**, 10330–10341.

58 R. H. Nie, H. X. Chen, Y. T. Yang, C. Li and H. M. Zhou, High-voltage layered manganese-based oxide cathode with excellent rate capability enabled by K/F co-doping, *ACS Appl. Energy Mater.*, 2023, **6**, 2358–2369.

59 S. Liu, Z. P. Liu, X. Shen, X. L. Wang, S. C. Liao, R. C. Yu, Z. X. Wang, Z. W. Hu, C. T. Chen, X. Q. Yu, X. Q. Yang and L. Q. Chen, Li-Ti cation mixing enhanced structural and performance stability of Li-rich layered oxide, *Adv. Energy Mater.*, 2019, **9**, 1901530–1901539.

60 G. Wang, C. H. Xie, H. Wang, Q. Li, F. J. Xia, W. H. Zeng, H. Y. Peng, G. Tendeloo, G. J. Tan, J. S. Tian and J. S. Wu, Mitigated oxygen loss in lithium-rich manganese-based cathode enabled by strong Zr-O affinity, *Adv. Funct. Mater.*, 2024, **34**, 2313672–2313681.

61 X. Li, K. J. Zhang, D. Mitlin, Z. Z. Yang, M. S. Wang, Y. Tang, F. Jiang, Y. G. Du and J. M. Zheng, Fundamental insight into Zr modification of Li- and Mn-rich cathodes: Combined transmission electron microscopy and electrochemical impedance spectroscopy study, *Chem. Mater.*, 2018, **30**, 2566–2573.

62 S. Liu, Z. P. Liu, X. Shen, W. H. Li, Y. R. Gao, M. N. Banis, M. S. Li, K. Chen, L. Zhu, R. C. Yu, Z. X. Wang, X. L. Sun, G. Lu, Q. Y. Kong, X. D. Bai and L. Q. Chen, Surface doping to enhance structural integrity and performance of Li-rich layered oxide, *Adv. Energy Mater.*, 2018, **8**, 1802105–1802112.

63 S. D. Dong, Y. Zhou, C. X. Hai, J. B. Zeng, Y. X. Sun, Y. Shen, X. Li, X. F. Ren, C. Sun, G. T. Zhang and Z. W. Wu, Understanding electrochemical performance improvement with Nb doping in lithium-rich manganese-based cathode materials, *J. Power Sources*, 2020, **462**, 228185–228193.

64 J. Z. Li, Y. W. Tian and C. Q. Xu, Influence of Nb^{5+} doping on structure and electrochemical properties of spinel Li1.02Mn2O4, *J. Mater. Sci. Technol.*, 2012, **28**, 817–822.

65 L. Zhang, T. Yuan, L. Soule, H. Sun, Y. P. Pang, J. H. Yang and S. Y. Zheng, Enhanced ionic transport and structural stability of Nb-doped O3-$NaFe_{0.55}Mn_{0.45-x}Nb_xO_2$ cathode material for long-lasting sodium ion batteries, *ACS Appl. Energy Mater.*, 2020, **3**, 3770–3778.

66 L. J. Wang, Y. Z. Wang, J. B. Zhao, Y. H. Li, J. L. Wang and X. H. Yang, Nb^{5+}-doped P2-type Mn-based layered oxide cathode with an excellent high-rate cycling stability for sodium-ion batteries, *Ionics*, 2019, **25**, 4775–4786.

67 P. H. Yang, S. C. Zhang, Z. W. Wei, X. G. Guan, J. Xia, D. Y. Huang, Y. L. Xing, J. He, B. H. Wen, B. Liu and H. Z. Xu, A gradient doping strategy toward superior electrochemical performance for Li-rich Mn-based cathode materials, *Small*, 2023, **29**, 2207797–2207106.

68 P. K. Nayak, J. Grinblat, M. Levi, E. Levi, S. Kim, J. W. Choi and D. Aurbach, Al doping for mitigating the capacity fading and voltage decay of layered Li and Mn-rich cathodes for Li-ion batteries, *Adv. Energy Mater.*, 2016, **6**, 1502398–1502410.

69 W. L. Pang, X. H. Zhang, J. Z. Guo, J. Y. Li, X. Yan, B. H. Hou, H. Y. Guan and X. L. Wu, P2-type $Na_{2/3}Mn_{1-x}Al_xO_2$ cathode material for sodium-ion batteries: Al-doped enhanced electrochemical properties and studies on the electrode kinetics, *J. Power Sources*, 2017, **356**, 80–88.

70 B. H. Song, C. F. Zhou, H. L. Wang, H. W. Liu, Z. W. Liu, M. O. Lai and L. Lu, Advances in sustain stable voltage of Cr-doped Li-rich layered cathodes for lithium ion batteries, *J. Electrochem. Soc.*, 2014, **161**, A1723–A1730.

71 X. Jin, Q. J. Xu, H. M. Liu, X. L. Yuan and Y. Y. Xia, Excellent rate capability of Mg doped $Li[Li_{0.2}Ni_{0.13}Co_{0.13}Mn_{0.54}]O_2$ cathode material for lithium-ion battery, *Electrochim. Acta*, 2014, **136**, 19–26.

72 H. R. Yao, P. F. Wang, Y. Gong, J. N. Zhang, X. Q. Yu, L. Gu, C. Y. Ouyang, Y. X. Yin, E. Y. Hu, X. Q. Yang, E. Stavitski, Y. G. Guo and L. J. Wan, Designing air-stable O3-type cathode materials by combined structure modulation for Na-ion batteries, *J. Am. Chem. Soc.*, 2017, **139**, 8440–8443.

73 S. N. Lim, J. Y. Seo, D. S. Jung, S. B. Park and S. H. Yeon, The crystal structure and electrochemical performance of $Li_{1.167}Mn_{0.548}Ni_{0.18}Co_{0.105}O_2$ composite cathodes doped and co-doped with Mg and F, *J. Electroanal. Chem.*, 2015, **740**, 88–94.

74 J. An, L. Y. Shi, G. R. Chen, M. S. Li, H. J. Liu, S. Yuan, S. M. Chen and D. S. Zhang, Insights into the stable layered structure of a Li-rich cathode material for lithium-ion batteries, *J. Mater. Chem. A*, 2017, **5**, 19738–19744.

75 S. N. Lim, J. Y. Seo, D. S. Jung, W. Ahn, H. S. Song, S. H. Yeon and S. B. Park, Rate capability for Na-doped $Li_{1.167}Ni_{0.18}Mn_{0.548}Co_{0.105}O_2$ cathode material and characterization of Li-ion diffusion using galvanostatic intermittent titration technique, *J. Alloys Compd.*, 2015, **623**, 55–61.

76 G. R. Chen, J. An, Y. M. Meng, C. Z. Yuan, B. Matthews, F. Dou, L. Y. Shi, Y. F. Zhou, P. A. Song, G. Wu and D. S. Zhang, Cation and anion co-doping synergy to improve structural stability of Li- and Mn-rich layered cathode materials for lithium-ion batteries, *Nano Energy*, 2019, **57**, 157–165.

77 X. Zhang, S. Q. Liu, B. Y. Wang, G. Q. Wang, H. Z. Du, X. Y. Wang, H. D. Zhang, S. Zhao, L. Wang and H. J. Yu,

Mn-based cathode materials for rechargeable batteries, *Sci. China Chem.*, 2023, **67**, 87–105.

78 Y. H. Liu, X. Fang, A. Y. Zhang, C. F. Shen, Q. Z. Liu, H. A. Enaya and C. W. Zhou, Layered P2-$Na_{2/3}[Ni_{1/3}Mn_{2/3}]O_2$ as high-voltage cathode for sodium-ion batteries: The capacity decay mechanism and Al_2O_3 surface modification, *Nano Energy*, 2016, **27**, 27–34.

79 Y. L. Qiao, Z. Zhou, Z. X. Chen, S. C. Du, Q. Cheng, H. W. Zhai, N. J. Fritz, Q. Du and Y. Yang, Visualizing ion diffusion in battery systems by fluorescence microscopy: A case study on the dissolution of $LiMn_2O_4$, *Nano Energy*, 2018, **45**, 68–74.

80 X. F. Zhang, I. Belharouak, L. Li, Y. Lei, J. W. Elam, A. M. Nie, X. Q. Chen, R. S. Yassar and R. L. Axelbaum, Structural and electrochemical study of Al_2O_3 and TiO_2 coated $Li_{1.2}Ni_{0.13}Mn_{0.54}Co_{0.13}O_2$ cathode material using ALD, *Adv. Energy Mater.*, 2013, **3**, 1299–1307.

81 S. J. Shi, J. P. Tu, Y. Y. Tang, X. Y. Liu, Y. Q. Zhang, X. L. Wang and C. D. Gu, Enhanced cycling stability of Li$[0.2Mn_{0.54}Ni_{0.13}Co_{0.13}]O_2$ by surface modification of MgO with melting impregnation method, *Electrochim. Acta*, 2013, **88**, 671–679.

82 B. Qiu, J. Wang, Y. G. Xia, Z. Wei, S. J. Han and Z. P. Liu, Enhanced electrochemical performance with surface coating by reactive magnetron sputtering on lithium-rich layered oxide electrodes, *ACS Appl. Mater. Interfaces*, 2014, **6**, 9185–9193.

83 J. T. Sun, Z. H. Zheng, W. C. Xia, L. Zhou, Y. N. Wei and F. L. Bei, Preparation of CeO_2-coated $Li_{1.2}Mn_{0.54}Co_{0.13}Ni_{0.13}O_2$ as cathode materials for lithium ion batteries, *Int. J. Electrochem. Sci.*, 2022, **17**, 221265–221277.

84 J. Lu, C. Zhan, T. P. Wu, J. G. Wen, Y. Lei, A. J. Kropf, H. M. Wu, D. J. Miller, J. W. Elam, Y. K. Sun, X. P. Qiu and K. Amine, Effectively suppressing dissolution of manganese from spinel lithium manganate via a nanoscale surface-doping approach, *Nat. Commun.*, 2014, **5**, 5693–5700.

85 Z. F. Li, X. Ren, W. C. Tian, Y. Zheng, L. W. An, J. C. Sun, R. Q. Ding, L. Z. Wen, L. Wang and G. C. Liang, $LiMn_{0.6}Fe_{0.4}PO_4$/CA cathode materials with carbon aerogel as additive synthesized by wet ball-milling combined with spray drying, *J. Electrochem. Soc.*, 2020, **167**, 090516–090525.

86 M. Chen, G. G. Zhang, B. H. Wu, M. Z. Liu, J. K. Chen, W. J. Xiang and W. S. Li, N-doped graphene-modified Li-rich layered $Li_{1.2}Mn_{0.6}Ni_{0.2}O_2$ cathode for high-performance Li-ion batteries, *ACS Appl. Energy Mater.*, 2022, **5**, 4307–4317.

87 M. Hallot, B. Caja-Munoz, C. Leviel, O. I. Lebedev, R. Retoux, J. Avila, P. Roussel, M. C. Asensio and C. Lethien, Atomic layer deposition of a nanometer-thick Li_3PO_4 protective layer on $LiNi_{0.5}Mn_{1.5}O_4$ films: Dream or reality for long-term cycling?, *ACS Appl. Mater. Interfaces*, 2021, **13**, 15761–15773.

88 S. X. Deng, B. W. Xiao, B. Q. Wang, X. Li, K. Kaliyappan, Y. Zhao, A. Lushington, R. Y. Li, T. K. Sham, H. Wang and X. L. Sun, New insight into atomic-scale engineering of electrode surface for long-life and safe high voltage lithium ion cathodes, *Nano Energy*, 2017, **38**, 19–27.

89 P. Vanaphuti, Y. T. Liu, X. T. Ma, J. Z. Fu, Y. L. Lin, J. G. Wen, Z. Z. Yang and Y. Wang, Stabilized lithium, manganese-rich layered cathode materials enabled by integrating co-doping and nanocoating, *ACS Appl. Mater. Interfaces*, 2021, **13**, 22597–22607.

90 R. D. L. Sandaruwan, L. N. Cong, L. P. Ma, S. C. Ma and H. Y. Wang, Tackling the interfacial issues of spinel $LiNi_{0.5}Mn_{1.5}O_4$ by room temperature spontaneous dediazonation reaction, *ACS Appl. Mater. Interfaces*, 2021, **13**, 13264–13272.

91 E. Y. Zhao, X. F. Liu, Z. B. Hu, L. M. Sun and X. L. Xiao, Facile synthesis and enhanced electrochemical performances of Li_2TiO_3-coated lithium-rich layered $Li_{1.13}Ni_{0.30}Mn_{0.57}O_2$ cathode materials for lithium-ion batteries, *J. Power Sources*, 2015, **294**, 141–149.

92 S. J. Hu, Y. Li, Y. H. Chen, J. M. Peng, T. F. Zhou, W. K. Pang, C. Didier, V. K. Peterson, H. Q. Wang, Q. Y. Li and Z. P. Guo, Insight of a phase compatible surface coating for long-durable Li-rich layered oxide cathode, *Adv. Energy Mater.*, 2019, **9**, 1901795–1901804.

93 X. W. Miao, H. Ni, H. Zhang, C. G. Wang, J. H. Fang and G. Yang, Li_2ZrO_3-coated $0.4Li_2MnO_3 \cdot 0.6LiNi_{1/3}Co_{1/3}Mn_{1/3}O_2$ for high performance cathode material in lithium-ion battery, *J. Power Sources*, 2014, **264**, 147–154.

94 P. F. Yan, J. M. Zheng, X. F. Zhang, R. Xu, K. Amine, J. Xiao, J. G. Zhang and C. M. Wang, Atomic to nanoscale investigation of functionalities of an Al_2O_3 coating layer on a cathode for enhanced battery performance, *Chem. Mater.*, 2016, **28**, 857–863.

95 H. V. Ramasamy, P. N. Didwal, S. Sinha, V. Aravindan, J. Heo, C. J. Park and Y. Lee, Atomic layer deposition of Al_2O_3 on P2-$Na_{0.5}Mn_{0.5}Co_{0.5}O_2$ as interfacial layer for high power sodium-ion batteries, *J. Colloid Interface Sci.*, 2020, **564**, 467–477.

96 M. M. Zhou, J. J. Zhao, Q. S. Tao, F. Tian, O. Potapenko, S. W. Zhong, H. Potapenko and Z. Liang, Structural and electrochemical properties of $Li_{1.2}Ni_{0.16}Mn_{0.54}Co_{0.08}O_2$-$Al_2O_3$ composite prepared by atomic layer deposition as the cathode material for LIBs, *Int. J. Electrochem. Sci.*, 2020, **15**, 10759–10771.

97 F. H. Zheng, Q. Deng, W. T. Zhong, X. Ou, Q. C. Pan, Y. Z. Liu, X. H. Xiong, C. H. Yang, Y. Chen and M. L. Liu, Fluorine-doped carbon surface modification of Li-rich layered oxide composite cathodes for high performance lithium-ion batteries, *ACS Sustain. Chem. Eng.*, 2018, **6**, 16399–16411.

98 Q. Y. Wang, J. Liu, A. V. Murugan and A. Manthiram, High capacity double-layer surface modified Li$[Li_{0.2}Mn_{0.54}Ni_{0.13}Co_{0.13}]O_2$ cathode with improved rate capability, *J. Mater. Chem.*, 2009, **19**, 4965–4972.

99 A. M. Haregewoin, A. S. Wotango and B.-J. Hwang, Electrolyte additives for lithium ion battery electrodes: Progress and perspectives, *Energy Environ. Sci.*, 2016, **9**, 1955–1988.

100 J. W. Liu, X. Song, L. Zhou, S. Q. Wang, W. Song, W. Liu, H. L. Long, L. X. Zhou, H. M. Wu, C. Q. Feng and Z. P. Guo, Fluorinated phosphazene derivative – A promising electrolyte additive for high voltage lithium ion batteries: From electrochemical performance to corrosion mechanism, *Nano Energy*, 2018, **46**, 404–414.

101 H. J. Zhao, S. G. Hu, Y. C. Fan, Q. R. Wang, J. D. Li, M. M. Yuan, X. Z. Ma, J. Wang, H. Y. Shao and Y. H. Deng, Significance of electrolyte additive molecule structure in stabilizing interphase in $LiN_{i0.8}C_{o0.1}Mn_{0.1}O_2$/artificial graphite pouch cells at high temperature, *Energy Storage Mater.*, 2024, **65**, 103151–103164.

102 Z. H. Liang, F. Tian, G. Z. Yang and C. X. Wang, Enabling long-cycling aqueous sodium-ion batteries via Mn dissolution inhibition using sodium ferrocyanide electrolyte additive, *Nat. Commun.*, 2023, **14**, 3591–3600.

103 J. G. Han, C. Hwang, S. H. Kim, C. Park, J. Kim, G. Y. Jung, K. Baek, S. Chae, S. J. Kang, J. Cho, S. K. Kwak, H. K. Song and N. S. Choi, An antiaging electrolyte additive for high-energy-density lithium-ion batteries, *Adv. Energy Mater.*, 2020, **10**, 2000563–2000576.

104 P. Z. Kou, Z. G. Zhang, Z. Y. Wang, R. G. Zheng, Y. G. Liu, F. Lv and N. Xu, Opportunities and challenges of layered lithium-rich manganese-based cathode materials for high energy density lithium-ion batteries, *Energy Fuels*, 2023, **37**, 18243–18265.

105 X. W. Zheng, X. S. Wang, X. Cai, L. D. Xing, M. Q. Xu, Y. H. Liao, X. P. Li and W. S. Li, Constructing a protective interface film on layered lithium-rich cathode using an electrolyte additive with special molecule structure, *ACS Appl. Mater. Interfaces*, 2016, **8**, 30116–30125.

106 Y. J. Wang, S. R. Cai, Z. Q. Sun, Q. Hou, H. H. Huang, J. C. Cheng, J. M. Fan, M. S. Zheng and Q. F. Dong, An active-oxygen-scavenging oriented cathode-electrolyte-interphase for long-life lithium-rich cathode materials, *Small*, 2022, **18**, 2106072–2106081.

107 Z. Z. Liu, Z. S. Liu, K. H. Li, X. Z. Zhao, M. M. Chen, H. Miao and L. Xia, Exploring trimethyl-phosphate-based electrolytes without a carbonyl group for Li-rich layered oxide positive electrodes in lithium-ion batteries, *J. Phys. Chem. Lett.*, 2022, **13**, 11307–11316.

108 Y. B. Liu, L. Tan and L. Li, Tris(trimethylsilyl) borate as an electrolyte additive to improve the cyclability of $LiMn_2O_4$ cathode for lithium-ion battery, *J. Power Sources*, 2013, **221**, 90–96.

109 M. Q. Xu, Y. Liang, B. Li, L. D. Xing, Y. Wang and W. S. Li, Tris (pentafluorophenyl) phosphine: A dual functionality additive for flame-retarding and sacrificial oxidation on $LiMn_2O_4$ for lithium ion battery, *Mater. Chem. Phys.*, 2014, **143**, 1048–1054.

110 Y. Sun, J. Huang, H. F. Xiang, X. Liang, Y. Z. Feng and Y. Yu, 2-(Trifluoroacetyl) thiophene as an electrolyte additive for high-voltage lithium-ion batteries using $LiCoO_2$ cathode, *J. Mater. Sci. Technol.*, 2020, **55**, 198–202.

111 S. Q. Li, X. R. Song, P. W. Jing, X. Y. Xiao, Y. C. Chen, Q. Sun, M. X. Huang, Y. P. Zhang, G. S. Li, P. Y. Liu, S. Xu, Q. Y. Dou, J. Zhu and X. B. Yan, Trace $NaBF_4$ modulated ultralow-concentration ether electrolyte for durable high-voltage sodium-ion batteries, *Adv. Funct. Mater.*, 2025, 2422491–2422500, DOI: 10.1002/adfm.202422491.

112 Y. K. Li, R. X. Zhang, J. S. Liu and C. W. Yang, Effect of heptamethyldisilazane as an additive on the stability performance of $LiMn_2O_4$ cathode for lithium-ion battery, *J. Power Sources*, 2009, **189**, 685–688.

113 H. Yamane, T. Inoue, M. Fujita and M. Sano, A causal study of the capacity fading of $Li_{1.01}Mn_{1.99}O_4$ cathode at 80°C, and the suppressing substances of its fading, *J. Power Sources*, 2001, **99**, 60–65.

114 F. Y. Cheng, J. Hu, W. Zhang, B. Y. Guo, P. Yu, X. L. Sun and J. Peng, Reviving ether-based electrolytes for sodium-ion batteries, *Energy Environ. Sci.*, 2025, **18**, 6874–6898.

115 Z. P. Jiang, T. Yang, C. Li, J. H. Zou, H. X. Yang, Q. G. Zhang and Y. T. Li, Synergistic additives enabling stable cycling of ether electrolyte in 4.4 V Ni-rich/Li metal batteries, *Adv. Funct. Mater.*, 2023, **33**, 2306868–2306876.

116 D. S. Hall, T. Hynes, C. P. Aiken and J. R. Dahn, Synthesis and evaluation of difluorophosphate salt electrolyte additives for lithium-ion batteries, *J. Electrochem. Soc.*, 2020, **167**, 100538–100545.

117 X. H. Liu, J. H. Zhao, H. H. Dong, L. L. Zhang, H. Zhang, Y. Gao, X. Z. Zhou, L. H. Zhang, L. Li, Y. Liu, S. C. Chou, W. H. Lai, C. F. Zhang and S. L. Chou, Sodium difluoro(oxalato)borate additive-induced robust SEI and CEI Layers enable dendrite-free and long-cycling sodium-ion batteries, *Adv. Funct. Mater.*, 2024, **34**, 2402310–2402319.

118 S. Wan, K. M. Song, J. C. Chen, S. S. Zhao, W. T. Ma, W. H. Chen and S. M. Chen, Reductive competition effect-derived solid electrolyte interphase with evenly scattered inorganics enabling ultrahigh rate and long-life span sodium metal batteries, *J. Am. Chem. Soc.*, 2023, **145**, 21661–21671.

119 Z. Li, L. P. Hou, N. Yao, X. Y. Li, Z. X. Chen, X. Chen, X. Q. Zhang, B. Q. Li and Q. Zhang, Correlating polysulfide solvation structure with electrode kinetics towards long-cycling lithium-sulfur batteries, *Angew. Chem., Int. Ed.*, 2023, **62**, e202309968–e202309976.

120 Y. G. Zou, B. D. Zhang, H. Y. Luo, X. Y. Yu, M. L. Yang, Q. Z. Zheng, J. H. Wang, C. Y. Jiao, Y. L. Chen, H. T. Zhang, J. Y. Xue, X. X. Kuai, H. G. Liao, C. Y. Ouyang, Z. Y. Ning, Y. Qiao and S. G. Sun, Electrolyte solvation engineering stabilizing anode-free sodium metal battery with 4.0 V-class layered oxide cathode, *Adv. Mater.*, 2024, **36**, 2410261–2410272.

121 S. M. Chen, Z. K. Deng, J. X. Li, W. G. Zhao, B. W. Nan, Y. Zuo, J. J. Fang, Y. X. Huang, Z. W. Yin, F. Pan and L. Y. Yang, Tuning reaction kinetics of fluorinated molecules to construct robust solid electrolyte interphases on SiOx anode, *Angew. Chem., Int. Ed.*, 2024, **64**, e202413927–e202413936.

122 Y. X. Li, W. K. Li, R. Shimizu, D. Cheng, H. Nguyen, J. Paulsen, S. Kumakura, M. H. Zhang and Y. S. Meng, Elucidating the effect of borate additive in high-voltage

electrolyte for Li-rich layered oxide materials, *Adv. Energy Mater.*, 2022, **12**, 2103033–2103045.

123 B. Koo, J. Lee, Y. Lee, J. K. Kim and N. S. Choi, Vinylene carbonate and tris(trimethylsilyl) phosphite hybrid additives to improve the electrochemical performance of spinel lithium manganese oxide/graphite cells at 60 °C, *Electrochim. Acta*, 2015, **173**, 750–756.

124 H. C. Guo, Z. Wei, K. Jia, B. Qiu, C. Yin, F. Q. Meng, Q. H. Zhang, L. Gu, S. J. Han, Y. Liu, H. Zhao, W. Jiang, H. F. Cui, Y. G. Xia and Z. P. Liu, Abundant nanoscale defects to eliminate voltage decay in Li-rich cathode materials, *Energy Storage Mater.*, 2019, **16**, 220–227.

125 B. Qiu, M. H. Zhang, L. J. Wu, J. Wang, Y. G. Xia, D. N. Qian, H. D. Liu, S. Hy, Y. Chen, K. An, Y. M. Zhu, Z. P. Liu and Y. S. Meng, Gas-solid interfacial modification of oxygen activity in layered oxide cathodes for lithium-ion batteries, *Nat. Commun.*, 2016, **7**, 12108–12117.

126 W. K. Pang, S. Kalluri, V. K. Peterson, N. Sharma, J. Kimpton, B. Johannessen, H. K. Liu, S. X. Dou and Z. P. Guo, Interplay between electrochemistry and phase evolution of the P2-type $Na_x(Fe_{1/2}Mn_{1/2})O_2$ cathode for use in sodium-ion batteries, *Chem. Mater.*, 2015, **27**, 3150–3158.

127 N. Yabuuchi, M. Kajiyama, J. Iwatate, H. Nishikawa, S. Hitomi, R. Okuyama, R. Usui, Y. Yamada and S. Komaba, P2-type $Na_x[Fe_{1/2}Mn_{1/2}]O_2$ made from earth-abundant elements for rechargeable Na batteries, *Nat. Mater.*, 2012, **11**, 512–517.

128 X. S. Liu, W. H. Zuo, B. Z. Zheng, Y. X. Xiang, K. Zhou, Z. M. Xiao, P. Z. Shan, J. W. Shi, Q. Li, G. M. Zhong, R. Q. Fu and Y. Yong, P2-$Na_{0.67}Al_xMn_{1-x}O_2$: Cost-effective, stable and high-rate sodium electrodes by euppressing phase transitions and enhancing sodium cation mobility, *Angew. Chem., Int. Ed.*, 2019, **58**, 18086–18095.

129 E. Talaie, V. Duffort, H. L. Smith, B. Fultz and L. F. Nazar, Structure of the high voltage phase of layered P2-Na2/3-z [Mn1/2Fe1/2]O2 and the positive effect of Ni substitution on its stability, *Energy Environ. Sci.*, 2015, **8**, 2512–2523.

130 Q. Y. Shen, Y. C. Liu, L. F. Jiao, X. H. Qu and J. Chen, Current state-of-the-art characterization techniques for probing the layered oxide cathode materials of sodium-ion batteries, *Energy Storage Mater.*, 2021, **35**, 400–430.

131 L. T. Zheng, L. J. Li, R. Shunmugasundaram and M. N. Obrovac, Effect of controlled-atmosphere storage and ethanol rinsing on $NaNi_{0.5}Mn_{0.5}O_2$ for sodium-ion batteries, *ACS Appl. Mater. Interfaces*, 2018, **10**, 38246–38254.

132 W. H. Zuo, J. M. Qiu, X. S. Liu, F. C. Ren, H. D. Liu, H. J. He, C. Luo, J. L. Li, G. F. Ortiz, D. H. Nan, J. P. Liu, M. S. Wang, Y. X. Li, R. Q. Fu and Y. Yang, The stability of P2-layered sodium transition metal oxides in ambient atmospheres, *Nat. Commun.*, 2020, **11**, 3544–3555.

133 X. Li, Y. Qiao, S. H. Guo, Z. M. Xu, H. Zhu, X. Y. Zhang, Y. Yuan, P. He, M. Ishida and H. S. Zhou, Direct visualization of the reversible O^{2-}/O^{-} redox process in Li-rich cathode materials, *Adv. Mater.*, 2018, **30**, 1705197–1705202.

134 X. Cao, H. F. Li, Y. Qiao, X. Li, M. Jia, J. Cabana and H. S. Zhou, Stabilizing reversible oxygen redox chemistry in layered oxides for sodium-ion batteries, *Adv. Energy Mater.*, 2020, **10**, 1903785–1903791.

135 E. Y. Hu, X. Q. Yu, R. Q. Lin, X. X. Bi, J. Lu, S. Bak, K. W. Nam, H. L. Xin, C. Jaye, D. A. Fischer, K. Amine and X. Q. Yang, Evolution of redox couples in Li- and Mn-rich cathode materials and mitigation of voltage fade by reducing oxygen release, *Nat. Energy*, 2018, **3**, 690–698.

136 M. Keller, T. Eisenmann, D. Meira, G. Aquilanti, D. Buchholz, D. Bresser and S. Passerini, In situ investigation of layered oxides with mixed structures for sodium-ion batteries, *Small Methods*, 2019, **3**, 1900239–1900248.

137 J. J. Marie, R. A. House, G. J. Rees, A. W. Robertson, M. Jenkins, J. Chen, S. Agrestini, M. Garcia-Fernandez, K. J. Zhou and P. G. Bruce, Trapped O_2 and the origin of voltage fade in layered Li-rich cathodes, *Nat. Mater.*, 2024, **23**, 818–825.

138 K. Luo, M. R. Roberts, R. Hao, N. Guerrini, D. M. Pickup, Y. S. Liu, K. Edström, J. H. Guo, A. V. Chadwick, L. C. Duda and P. G. Bruce, Charge-compensation in 3d-transition-metal-oxide intercalation cathodes through the generation of localized electron holes on oxygen, *Nat. Chem.*, 2016, **8**, 684–691.

139 K. H. Dai, J. P. Wu, Z. Q. Zhuo, Q. H. Li, S. Sallis, J. Mao, G. Ai, C. H. Sun, Z. Y. Li, W. E. Gent, W. C. Chueh, Y. D. Chuang, R. Zeng, Z. X. Shen, F. Pan, S. S. Yan, L. F. J. Piper, Z. Hussain, G. Liu and W. L. Yang, High reversibility of lattice oxygen redox quantified by direct bulk probes of both anionic and cationic redox reactions, *Joule*, 2019, **3**, 518–541.

140 S. Ivanova, E. Zhecheva, R. Kukeva, D. Nihtianova, L. Mihaylov, G. Atanasova and R. Stoyanova, Layered P3-$Na_xCo_{1/3}Ni_{1/3}Mn_{1/3}O_2$ versus spinel $Li_4Ti_5O_{12}$ as a positive and a negative electrode in a full sodium-lithium cell, *ACS Appl. Mater. Interfaces*, 2016, **8**, 17321–17333.

141 J. H. Jo, J. U. Choi, A. Konarov, H. Yashiro, S. Yuan, L. Y. Shi, Y. K. Sun and S. T. Myung, Sodium-ion batteries: Building effective layered cathode materials with long-term cycling by modifying the surface via sodium phosphate, *Adv. Funct. Mater.*, 2018, **28**, 1705968–1705978.

142 X. Y. Zhang, Y. Qiao, S. H. Guo, K. Z. Jiang, S. Xu, H. Xu, P. Wang, P. He and H. S. Zhou, Manganese-based Na-rich materials boost anionic redox in high-performance layered cathodes for sodium-ion batteries, *Adv. Mater.*, 2019, **31**, 1807770–1807778.

143 Y. R. Gao, X. F. Wang, J. Ma, Z. X. Wang and L. Q. Chen, Selecting substituent elements for Li-rich Mn-based cathode materials by density functional theory (DFT) calculations, *Chem. Mater.*, 2015, **27**, 3456–3461.

144 P. H. Xiao, Z. Q. Deng, A. Manthiram and G. Henkelman, Calculations of oxygen stability in lithium-rich layered cathodes, *J. Phys. Chem. C*, 2012, **116**, 23201–23204.

145 H. Chen and M. S. Islam, Lithium extraction mechanism in Li-rich Li_2MnO_3 involving oxygen hole formation and dimerization, *Chem. Mater.*, 2016, **28**, 6656–6663.

146 G. Assat and J. M. Tarascon, Fundamental understanding and practical challenges of anionic redox activity in Li-ion batteries, *Nat. Energy*, 2018, **3**, 373–386.
147 K. Flensberg, F. von Oppen and A. Stern, Engineered platforms for topological superconductivity and majorana zero modes, *Nat. Rev. Mater.*, 2021, **6**, 944–958.
148 X. H. Wan, Z. Y. Li, W. Yu, A. Y. Wang, X. Ke, H. L. Guo, J. H. Su, L. Li, Q. Z. Gui, S. P. Zhao, J. Robertson, Z. F. Zhang and Y. Z. Guo, Machine learning paves the way for high entropy compounds exploration: Challenges, progress, and outlook, *Adv. Mater.*, 2023, 2305192–2305217, DOI: 10.1002/adma.202305192.
149 Q. W. Cui, S. L. Yu, Y. Li, X. Y. Li, X. L. Zhao, W. J. Qiu and J. J. Liu, Modulating coupled polyhedral distortion in Li-rich cathodes for synergistically inhibiting capacity and voltage decay, *Adv. Mater.*, 2025, 2505616–2505626, DOI: 10.1002/adma.202505616.
150 Y. X. Zhou, Y. F. Ding, Y. Y. Chen, Y. L. Shen, Z. L. Wang, X. R. Li, J. J. Xu and X. Y. Huang, Thermal degradation of lithium-ion battery cathodes: A machine learning prediction of stability and safety, *Energy Mater.*, 2025, **5**, 500077–500098.
151 J. Kim, I. Choi, J. S. Kim, H. Hwang, B. Yu, S.-C. Nam and I. Park, Data-driven insights into the reaction mechanism of Li-rich cathodes, *Energy Environ. Sci.*, 2025, **18**, 4222–4230.
152 S. Rath, G. Sudha Priyanga, N. Nagappan and T. Thomas, Discovery of direct band gap perovskites for light harvesting by using machine learning, *Comp. Mater. Sci.*, 2022, **210**, 111476–111485.
153 G. Houchins and V. Viswanathan, An accurate machine-learning calculator for optimization of Li-ion battery cathodes, *J. Chem. Phys.*, 2020, **153**, 054124–054131.
154 G. Y. Wang, T. Fearn, T. Y. Wang and K. L. Choy, Machine-learning approach for predicting the discharging capacities of doped lithium nickel-cobalt-manganese cathode materials in Li-ion batteries, *ACS Cent. Sci.*, 2021, **7**, 1551–1560.
155 S. J. Yang, S. H. Hu, J. F. Zhao, H. W. Cui, Y. F. Wang, S. Zhao, C. F. Lan and Z. R. Dong, Prediction on discharging properties of nickel-manganese materials for high-performance sodium-ion batteries via machine learning methods, *Energy Technol.*, 2022, **10**, 2200733–2200739.
156 Y. H. Wan, B. Y. Huang, W. S. Liu, D. L. Chao, Y. G. Wang and W. Li, Fast-charging anode materials for sodium-ion batteries, *Adv. Mater.*, 2024, **36**, 2404574.
157 T. Z. Yang, D. Luo, X. Y. Zhang, S. H. Gao, R. Gao, Q. Y. Ma, H. W. Park, T. Or, Y. G. Zhang and Z. W. Chen, Sustainable regeneration of spent cathodes for lithium-ion and post-lithium-ion batteries, *Nat Sustainability*, 2024, **7**, 776–785.
158 T. Z. Yang, D. Luo, A. P. Yu and Z. W. Chen, Enabling future closed-loop recycling of spent lithium-ion batteries: Direct cathode regeneration, *Adv. Mater.*, 2023, **35**, 2203218–2203230.
159 A. Y. Zuo, H. J. Feng, T. Y. Yuan, J. Q. Gan, L. H. Xu, K. Q. Shu, Y. Luo, J. Tian, Z. J. Wang, K. Xue and D. H. Wang, Photo-driven selective recycling of spent $LiFePO_4$ batteries and valuable photocatalytic utilization of recovered ferrous oxalate, *J. Hazard. Mater.*, 2026, **501**, 140753–140766.
160 E. A. Olivetti, G. Ceder, G. G. Gaustad and X. K. Fu, Lithium-ion battery supply chain considerations: Analysis of potential bottlenecks in critical metals, *Joule*, 2017, **1**, 229–243.
161 X. J. Qiu, B. C. Zhang, Y. L. Xu, J. G. Hu, W. T. Deng, G. Q. Zou, H. S. Hou, Y. Yang, W. Sun, Y. H. Hu, X. Y. Cao and X. B. Ji, Enabling the sustainable recycling of $LiFePO_4$ from spent lithium-ion batteries, *Green Chem.*, 2022, **24**, 2506–2515.
162 X. P. Chen, L. Yuan, S. X. Yan and X. Ma, Self-activation of ferro-chemistry based advanced oxidation process towards in-situ recycling of spent $LiFePO_4$ batteries, *Chem. Eng. J.*, 2023, **471**, 144343–144352.
163 J. B. Dunn, L. Gaines, J. C. Kelly, C. James and K. G. Gallagher, The significance of Li-ion batteries in electric vehicle life-cycle energy and emissions and recycling's role in its reduction, *Energy Environ. Sci.*, 2015, **8**, 158–168.
164 X. L. Li, Z. Dai, Z. H. Xu, Q. W. Li, H. R. Liu, K. Lv and A. Bayaguud, High-voltage and high-capacity oxide cathode materials in sulfide-based all-solid-state lithium batteries, *J. Energy Storage*, 2025, **121**, 116504–116520.
165 Y. Dou, S. Y. Zhou, J. I. G. Dawkins, K. Zaghib, K. Amine, G. L. Xu and S. X. Deng, Manganese-based spinel cathodes: A promising frontier for solid-state lithium-ion batteries, *Adv. Mater.*, 2025, **38**, e14126.